

SUPPORTING INFORMATION

Tunable Synthesis of Nitrogen Doped Graphene from Fluorographene under Mild Conditions

Dagmar Zaoralová^{#†‡}, Vítězslav Hrubý^{#†‡}, Veronika Šedajová^{†‡}, Radim Mach^{†‡}, Vojtěch Kupka^{†‡}, Juri Ugolotti[†], Aristides Bakandritsos^{†}, Miroslav Medved^{*†} and Michal Otyepka^{*†‡}*

[#] These authors contributed equally to this work

[†] Regional Centre of Advanced Technologies and Materials, Faculty of Science, Palacký University in Olomouc, Šlechtitelů 27, 783 71 Olomouc, Czech Republic.

[‡] Department of Physical Chemistry, Faculty of Science, Palacký University in Olomouc, 17. listopadu 12, 771 46 Olomouc, Czech Republic.

Corresponding Authors

*Aristides Bakandritsos, e-mail: aristeidis.bakandritsos@upol.cz

*Miroslav Medved', email: miroslav.medved@upol.cz

*Michal Otyepka, email: michal.otyepka@upol.cz

Number of pages: 37

Number of figures: 34

Number of tables: 4

Number of schemes: 3

1. Experimental Section

Materials. Graphite, fluorinated, polymer (GrF, >61 wt. % F), *N,N*-dimethylformamide (DMF, anhydrous, 99.8 %), sodium amide (NaNH_2 , 98 %), acetone (p.a.), ethanol (p.a.), propylene carbonate (PC, anhydrous, 99.8 %), acetonitrile (ACN, HPLC grade) were obtained from Sigma Aldrich. *N,N*-dimethylformamide (DMF, p.a.) was purchased from Penta.

Synthesis of the nitrogen doped graphene (NG). Graphite fluoride (GrF, 0.5 g) was added in a 100mL two-neck round-bottom glass flask with septum and degassed three times using vacuum pump following backfilling the flask with nitrogen from the balloon via the three-way valve. Then, 30 mL of DMF was added into the flask via syringe through the septum and the mixture was degassed again for three times. The mixture was stirred for 2 days at room temperature under nitrogen atmosphere, then sonicated for 4 hours in sonicator bath (Bandelin Sonorex, DT 255H type) and stirred overnight. After this initial step, the GrF dispersion was transferred into the Teflon vessel and 1 g of sodium amide was added. Then, the inert-atmosphere apparatus with reflux condenser was set up, degassed for three times and the mixture was stirred and heated at 130 °C using oil bath for 1, 3 or 6 hours, 1 day, and 3 days. Additionally, reactions at 70 °C (NG70) and room temperature (NGrt) were also performed to test the influence of the temperature on the obtained products. After the mixture cooled down, solid materials were separated from the liquid by centrifugation (Sigma 4-16K) at 10 000 rcf for 5 minutes. The supernatant was collected for analysis and the black precipitate was purified by successive washing steps by dispersing it in fresh solvent with help of sonication and following centrifugation. Washings with DMF, acetone, ethanol and ultra-pure water (all 3×) consecutively, as well as hot DMF and hot water were performed. More washing steps using water were applied if the conductivity of the supernatant aqueous fraction was higher than 100 $\mu\text{S cm}^{-1}$. During the final centrifugation steps with water, maximum centrifugation forces (21 000 rcf) and prolonged centrifugation times had to be applied to isolate the product. Optionally, the dialysis of the aqueous dispersions was done instead of

centrifugation. After washing, the material was suspended in water or lyophilized, depending on the following characterization.

Similar procedures were followed for syntheses using different solvents performed on smaller scale, preserving the original molar ratios of the starting materials. Synthesis in propylene carbonate (PC) was performed with 100 mg of GrF, 200 mg of NaNH₂ and 6 mL of PC at 130 °C. For purification of the resultant material (NG_PC), PC and acetone was used for washing through centrifugation. For synthesis performed in acetonitrile (ACN), 200 mg of GrF, 400 mg of NaNH₂ and 12 mL of ACN was used. ACN was dried using molecular sieves prior to reaction. For the purification of ACN-resultant material (NG_ACN), ACN washing step was used instead of DMF.

Blank sample was prepared by thermal reduction of 0.5 g of GrF in 30 mL of DMF at 130 °C for 3 days in the same way as the synthesis of the main material. The resulting material (reduced FG, rFG) was purified, as in the case of NG product.

Characterization techniques. FT-IR spectra were recorded on an iS5 FTIR spectrometer (Thermo Nicolet) using the Smart Orbit ZnSe ATR accessory. Lyophilizate of the relevant material was placed on the ZnSe crystal and pressed. Acquired spectra were the sum of 16 scans, using nitrogen gas flow through the ATR accessory. Baseline corrections were applied to the collected spectra.

Raman spectra were recorded on a DXR Raman microscope using the 633 nm excitation line of a diode laser.

X-ray photoelectron spectroscopy (XPS) was employed with a PHI VersaProbe II (Physical Electronics) spectrometer using an Al K α source (15 kV, 50 W). Samples were deposited onto the silicon holder as a water-, ethanol- or acetone-based slurry that was let to dry prior to the measurement. The obtained data were evaluated and deconvoluted with the MultiPak (Ulvac - PHI, Inc.) software package. Spectral analysis included a Shirley background subtraction and peak deconvolution employing mixed Gaussian–Lorentzian functions. The spot

size of the sampling area was 100 μm and the take-off angle was 45°, thus providing information from >3 nm depth. Several batches of the final NG products were measured with error regarding the atomic composition determination of ~6%.

Scanning electron microscopy (SEM) images were taken using a Hitachi SU6600 instrument with accelerating voltage of 5 kV. Scanning transmission electron microscopy-high-angle annular dark-field imaging analyses for elemental mapping of the products were performed with a FEI Titan HRTEM (high-resolution TEM) microscope operating at 200 kV. For these analyses, a droplet of an aqueous dispersion of the material with a concentration of ~0.1 mg mL⁻¹ was deposited on a carbon-coated copper grid and slowly dried at room temperature.

Thermal analyses were performed with an STA449 C Jupiter Netzsch instrument at a heating rate of 10 °C min⁻¹, under a N₂ flow (100 ml min⁻¹) in the sample compartment.

Electro-kinetic measurements for the determination of the particles' mobility and zeta potential values were performed with a Malvern ZetaSizer Nano instrument. Each dispersion was diluted down to concentration around 0.2 mg mL⁻¹ prior to measurement and the final value was the mean of three measurements.

Surface area and pore size analysis was performed by means of N₂ adsorption/desorption measurements at 77 K and CO₂ measurements at 273 K on a volumetric gas adsorption analyzer (3Flex, Micromeritics, USA) up to 0.965 and 0.035 P/P₀ for N₂ and CO₂, respectively. Prior the analysis, the sample was degassed under high vacuum (10⁻⁴ Pa) at 130 °C for 12 hours, while high purity (99.999 %) N₂, CO₂ and He gases were used for the measurements. The Brunauer–Emmett–Teller area (BET) was determined with respect to Rouquerol criteria for N₂ isotherm, while Dubinin-Astakhov method was used for CO₂ micropore surface area determination. Pore size distribution was analyzed by N₂-NLDFT 77-carbon slit pore kernel and CO₂-NLDFT 273-carbon slit pore kernel.

The GC-MS analyses was carried out on an Agilent 7890 B gas chromatograph with DB-624 column (diameter 250 μm , length 30 m), and Agilent 5977 B mass spectrometer. Length of restrictor line was 2 meters and the transfer line was heated to 250 $^{\circ}\text{C}$. Helium gas was used both as a mobile phase and as a purge gas in the active splitter. Each DMF-based supernatant liquid was filtered through syringe microfilter prior to injection, when 0.5 μL of liquid was injected into the inlet with a split ratio of 20:1. The temperature of the inlet was 250 $^{\circ}\text{C}$. Initial oven temperature of 35 $^{\circ}\text{C}$ was held for 5 min and then increased by 20 $^{\circ}\text{C min}^{-1}$. The final temperature of 250 $^{\circ}\text{C}$ was held for 4 minutes making a total run time of the analysis 19.75 minutes. Flow through the column was set to 1.8 mL min^{-1} . The fragments were scanned in the range of 15 to 350 m/z values. MS was turned on 2.8 minutes after the injection, then turned off between 12.05 and 12.60 minutes to prevent DMF elution damaging ion source. Resulting mass spectra were processed through NIST/EPA/NIH Mass Spectral Database using the NIST MS Search Program and eluents were assigned to the compounds if their mass spectra had match factor higher than 700.

NMR spectra were collected using a JEOL spectrometer JNM-ECZ400R (^{13}C frequency 100.5 MHz). The ^{13}C spectra were measured in demineralised water.

2. Computational details

To compare stabilities of vacancies that may be present in fluorographene lattice, periodic boundary condition (PBC) calculations were performed. Spin-polarized density functional theory (DFT) with the Perdew, Burke and Ernzerhof functional with Grimme correction for weak interactions (PBE-D2)¹ and projected augmented wave potentials (PAW) representing atomic cores, as implemented in the Vienna ab initio simulation package (VASP)²⁻⁵ was used. The wave functions were expanded in the plane-wave basis set with a minimum cutoff of 400 eV. The Brillouin zone integrations were performed with $3\times 3\times 1$ Γ -centered Monkhorst-Pack k-point mesh⁶ per conventional 6×6 triclinic cell containing 72 carbon atoms. All optimized structures were converged to forces of less than 10^{-2} eV/ \AA , with a criterion 10^{-5} eV for each SCF cycle.

XPS binding energies of different nitrogen configurations were computed using FHI-aims code⁷ using the PBE functional⁸ in with the *light* basis set. K-point mesh was set to 4x4x1. The binding energies were calculated using the final state method as the difference of total energy of the system with a core hole and that of the ground state.

To explore possible reaction paths, calculations with Gaussian09⁹ program were performed. Ground state structures of all investigated species were optimized by the ω B97X-D¹⁰ method in combination with the 6-31++G(d,p) basis set.¹¹ For open-shell systems, the spin unrestricted formalism has been applied. The solvent effects were taken into account using the universal continuum solvation model based on electron density (SMD).¹²

To mimic the semilocal flexibility of FG sheets, the FG-like structures were obtained by constrained geometry optimizations keeping the edge carbon atoms frozen (Figure S1). In calculations related to aziridinic N formation and creation of new vacancies (Figure S20-22), and in calculations related to nucleophilic attack on SV and DV(14) (Figure 4), *trans*-dotetrakontafluorocircumpyrene (**c14**) was used as a model of FG. In calculations related to the expansion of already existing vacancies in FG lattice (Figure S34) *trans*-tetrapentakontafluorocircumcoronene (**c19**) was used.

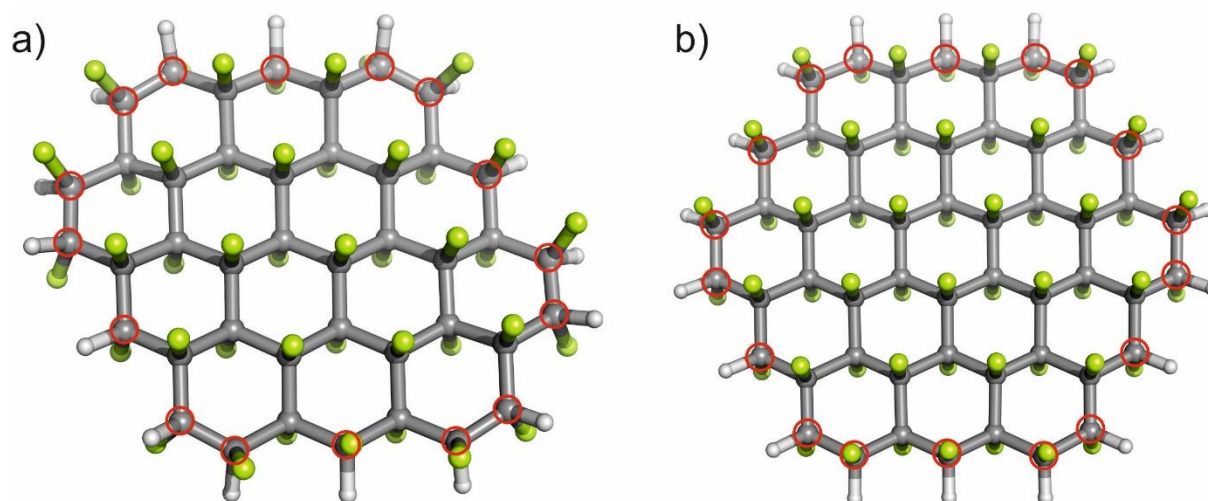


Figure S1. Models of FG that were used in calculations. a) *trans*-dotetrakontafluorocircumpyrene (**c14**) and b) *trans*-tetrapentakontafluorocircumcoronene (**c19**) Red marked carbon atoms were kept frozen during optimization calculations. Carbon atoms are grey, fluorine green and hydrogen white.

The cohesion energy of FG vacancies was calculated according to this equation

$$E_{coh} = \frac{E_{vacancy} - xE_C - yE_F}{x+y}, \quad (S1)$$

where $E_{vacancy}$ is the energy of the supercell of FG vacancy (C_xF_y), x is the number of carbon atoms in the supercell, E_C is energy carbon atom, y is the number of fluorine atoms in the supercell and E_F is energy of F atom.

3. Supplementary results on the synthesis and characterization of the NG material

From observation of the process, the reaction mixture turned from pale-grey into black immediately after addition of the sodium amide into the FG dispersion in DMF. The NG material was purified by described procedure with 1-week dialysis of the dispersion in UPW in 5 litres of distilled water that was replaced twice during the process. Final conductivity of the dispersion was $29.6 \mu S cm^{-1}$, its pH was 7.6 and zeta potential value at such pH was -19.4 mV.

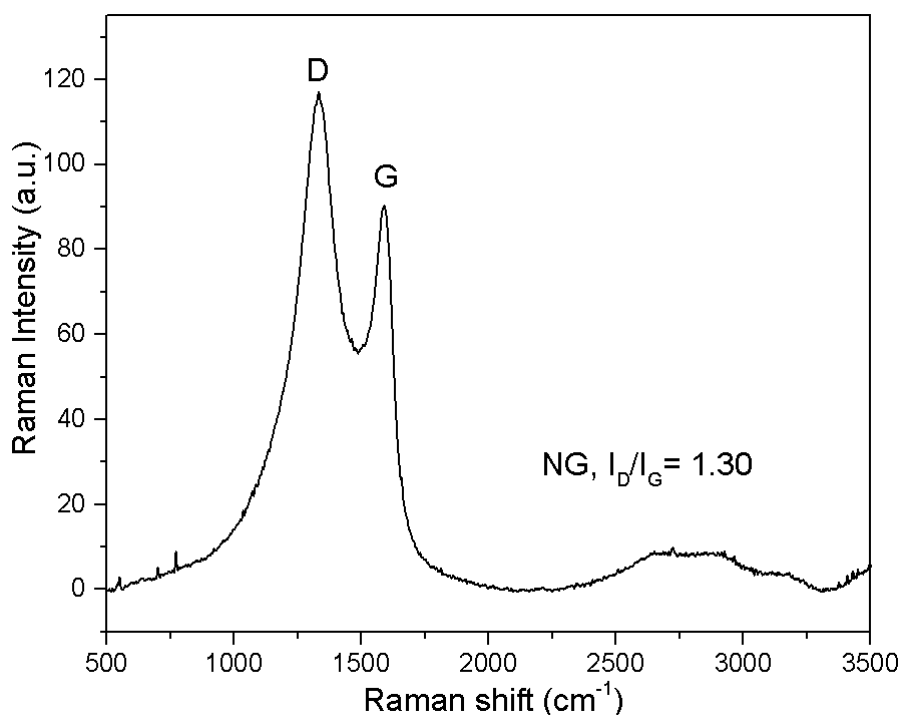


Figure S2. Raman spectrum of NG material with inset I_D/I_G ratio

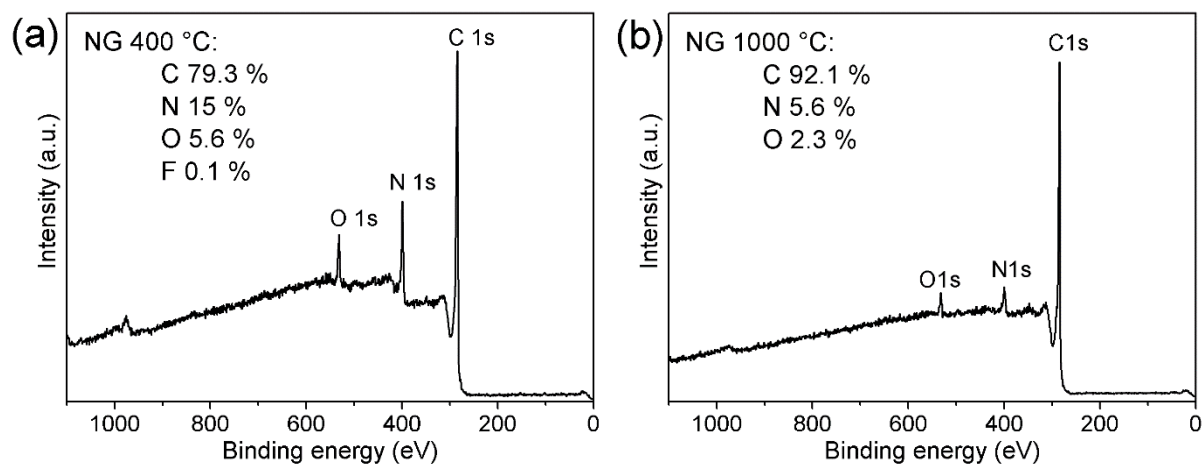


Figure S3. Survey XPS spectrum of NG withdrawn from thermal analysis (10 °C/min) at (a) 400 °C and (b) 1000 °C.

For ninhydrin testing (Figure S4), 0.2 g of ninhydrin was dissolved in 10 mL of acetone. Then, five drops of the solution were added to 0.7 mL of tested dispersion along with three drops of 1M NaOH. For the separation of the solid and liquid, the prepared mixture was centrifuged at 50000 rcf for 10 minutes.

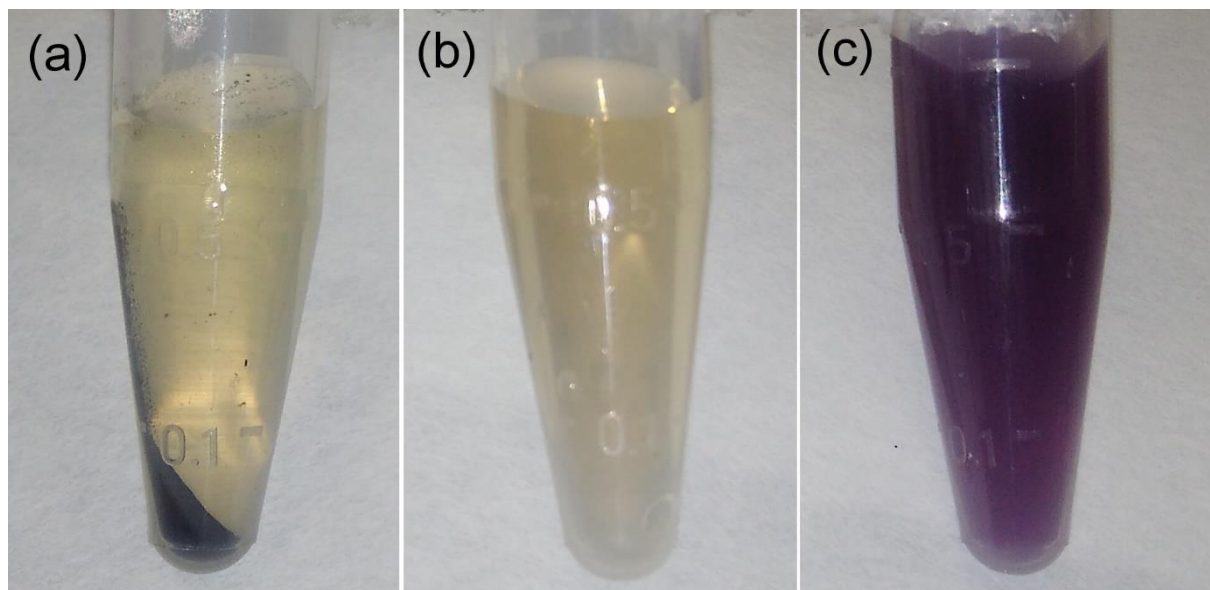


Figure S4. Ninhydrin tests of (a) NG material, (b) blank and (c) dodecylamine solution for comparison.

In order to further investigate the nitrogen configurations of the NG material, 15 mg of the material were three times washed using 10 mL of aqueous 2M HCl solution in order to protonate its nitrogen functionalities. Furthermore, another 15 mg were washed three times using aqueous 2M solution of NaOH and once with absolute ethanol. Both samples were then placed onto the silicon XPS holder without further treatment. The N 1s envelope of the protonated NG material, showed increased intensity of the component around 400 eV. This can

be ascribed, according to the theoretical studies, to protonation of pyridinic nitrogen configurations, when BE of the pyridinic nitrogen shifts from 398.5 eV to 400.5 eV.¹³

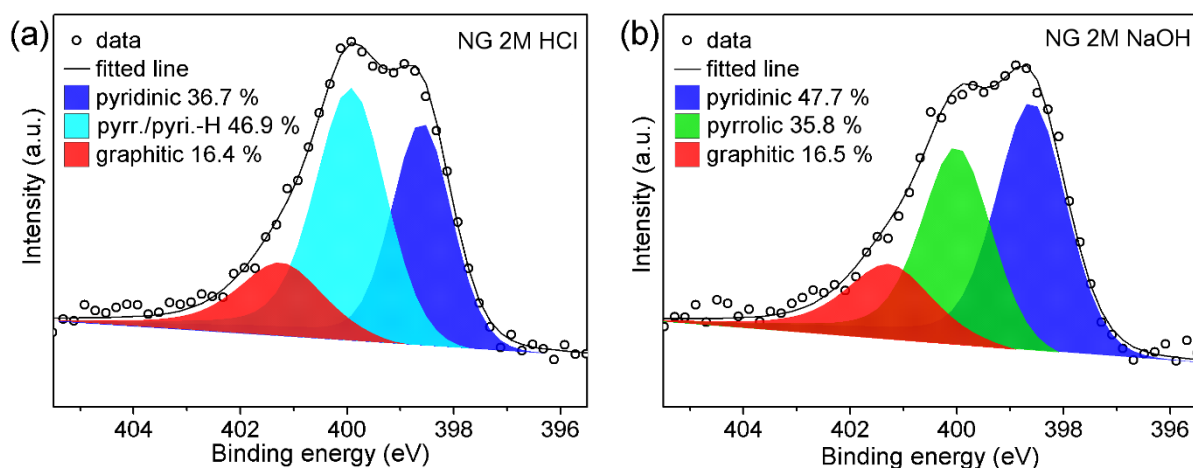


Figure S5. (a) Deconvolution of N 1s XPS pattern of NG treated with 2M HCl, and (b) deconvoluted N 1s pattern of NG treated with 2M NaOH and EtOH washing. It should be noted that the equilibrium between protonated-deprotonated pyridinic groups cannot be shifted 100 % to one side. As shown in panel (a), even after 3 times washing with 2M HCl solution (pH~0) and without further washing with other solvents, significant amount of deprotonated pyridinic groups remained. This was attributed to the drying of the sample before XPS measurement, and thus interaction with the water from environmental humidity, which can significantly shift the equilibrium back. For this reason, it was not possible to determine the exact amount of protonated pyridinic nitrogens, appearing at the same BE region as the pyrrolic ones.

For determination of zeta potential dependence on pH (Figure S6), the pH was adjusted by adding diluted solutions of HCl or NaOH.

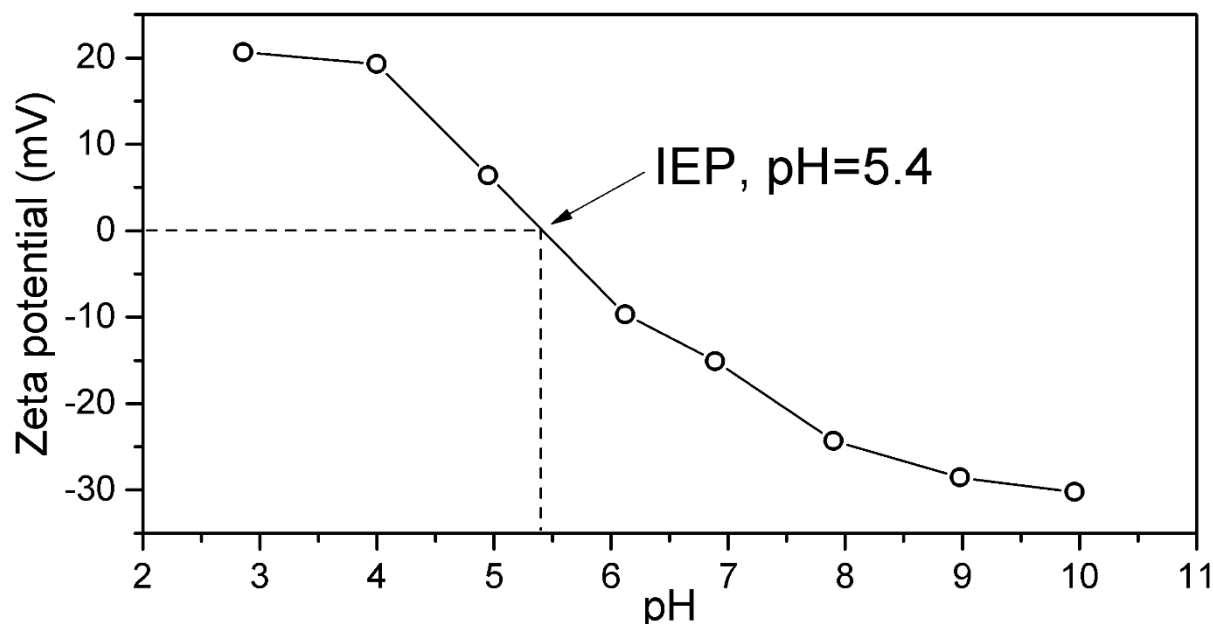


Figure S6. Dependence of zeta potential values on pH of NG dispersions for determination of the point of zero charge.

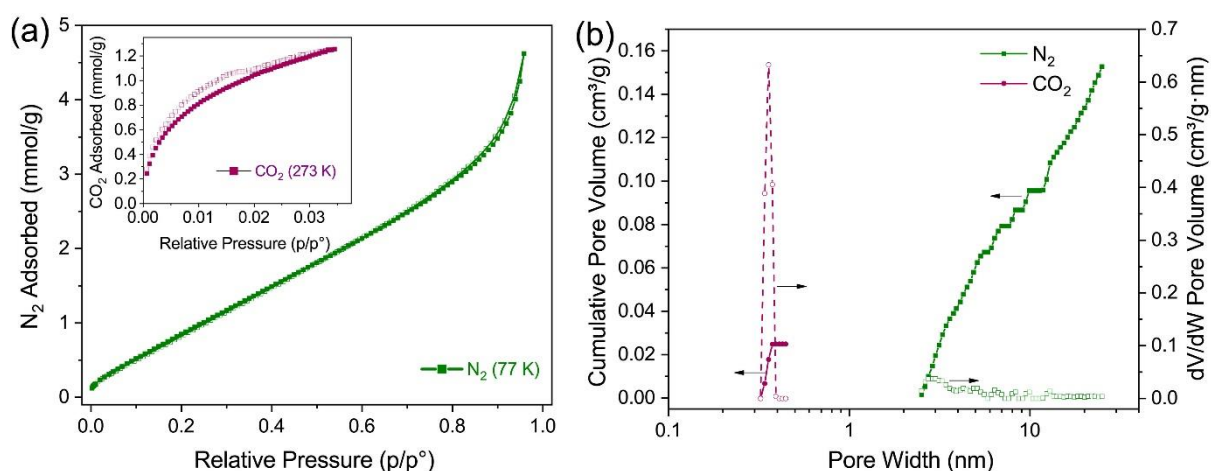


Figure S7. a) Gas adsorption/desorption isotherms for N₂ at 77 K and CO₂ at 273 K (inset) recorded for the final product (NG). b) Pore size distributions calculated from the previous recorded data analyzed by means of NLDFT slit pore kernels for N₂ and CO₂, respectively.

4. Supplementary data for materials synthesized under different conditions

A sample was isolated by withdrawing a small fraction of from the GrF/DMF reaction mixture after 3-day mixing and 4 h sonication. The sample was washed three times with acetone prior to deposition on the XPS holder (Figure S8).

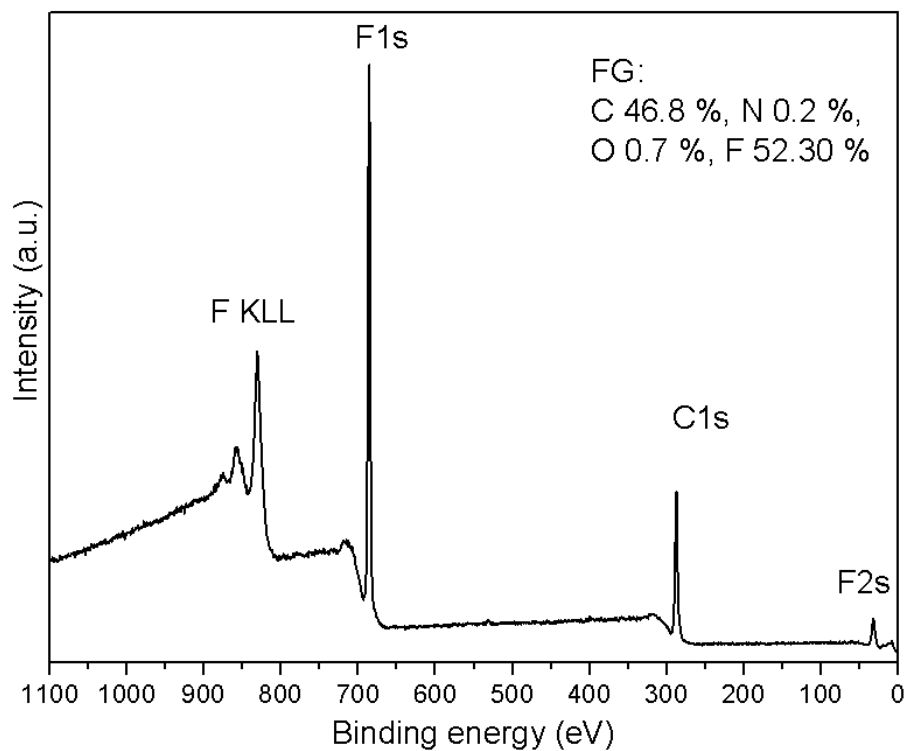


Figure S8. Survey XPS spectrum of FG material after 3-day mixing in DMF and 4 h sonication. The inset in right-hand corner shows the elemental atomic composition.

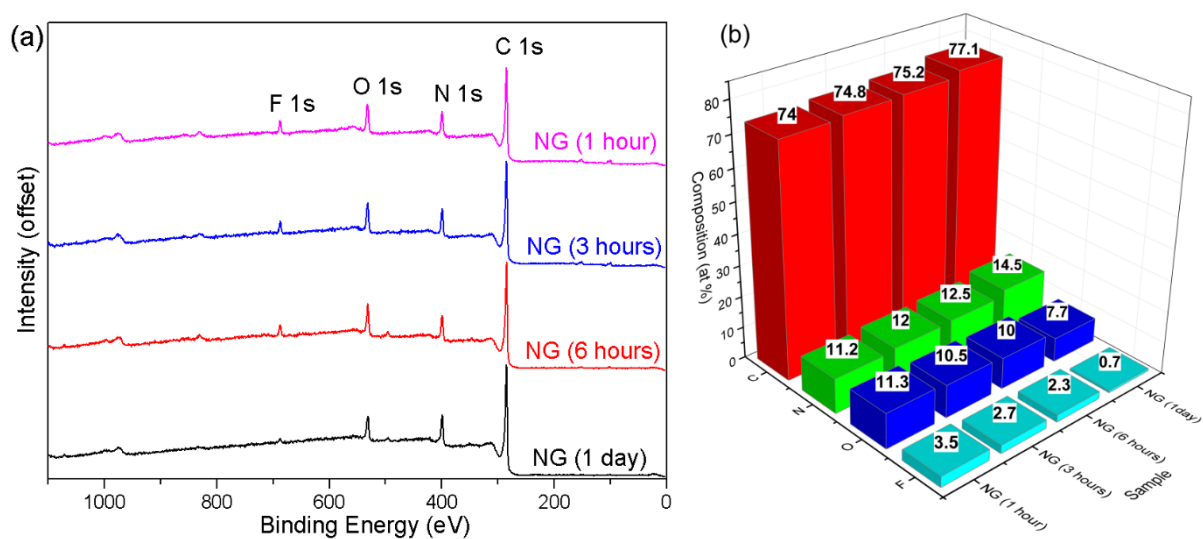


Figure S9. (a) Survey XPS spectra of NG products isolated at different reaction times and (b) corresponding atomic compositions.

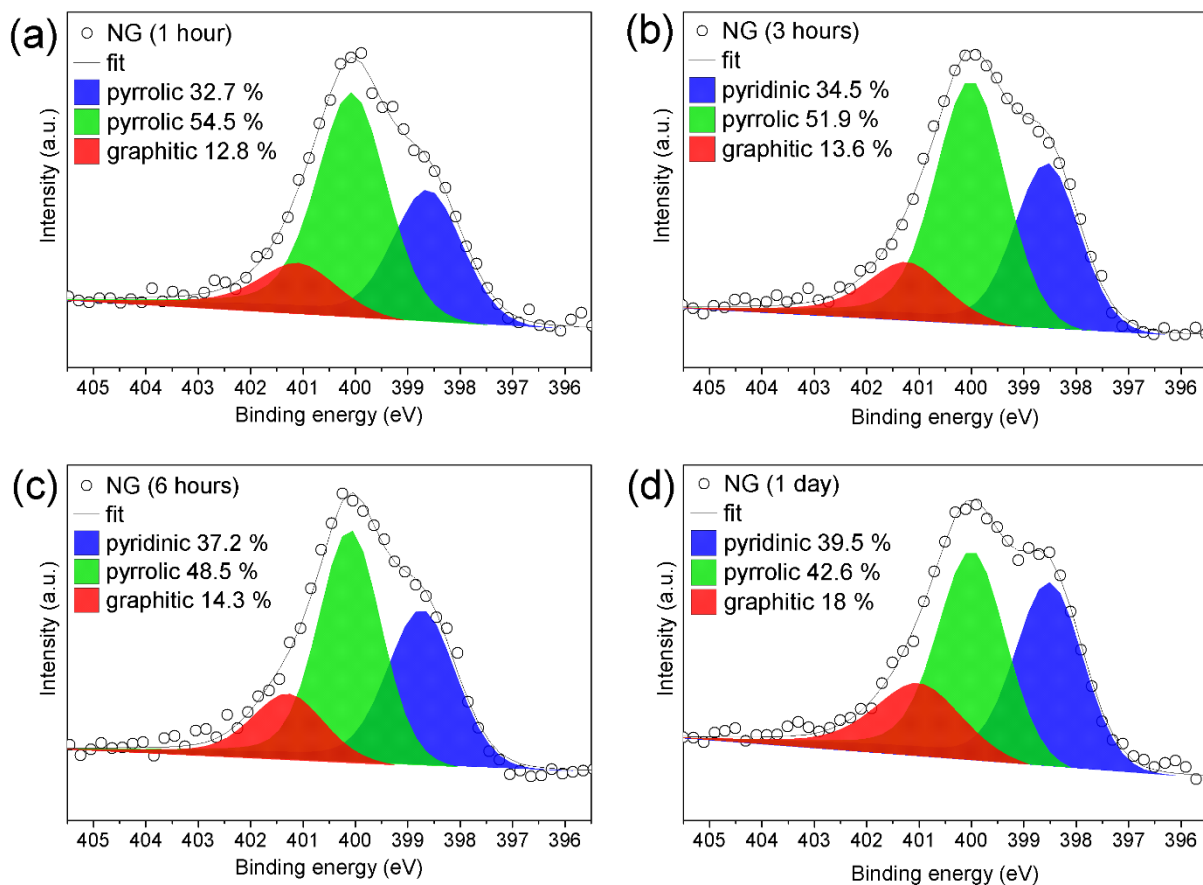


Figure S10. Deconvolution of N 1s envelope of NG products synthesized in DMF at 130 °C after (a) 1-hour reaction, (b) 3-hour reaction, (c) 6-hour reaction and (d) 1-day reaction.

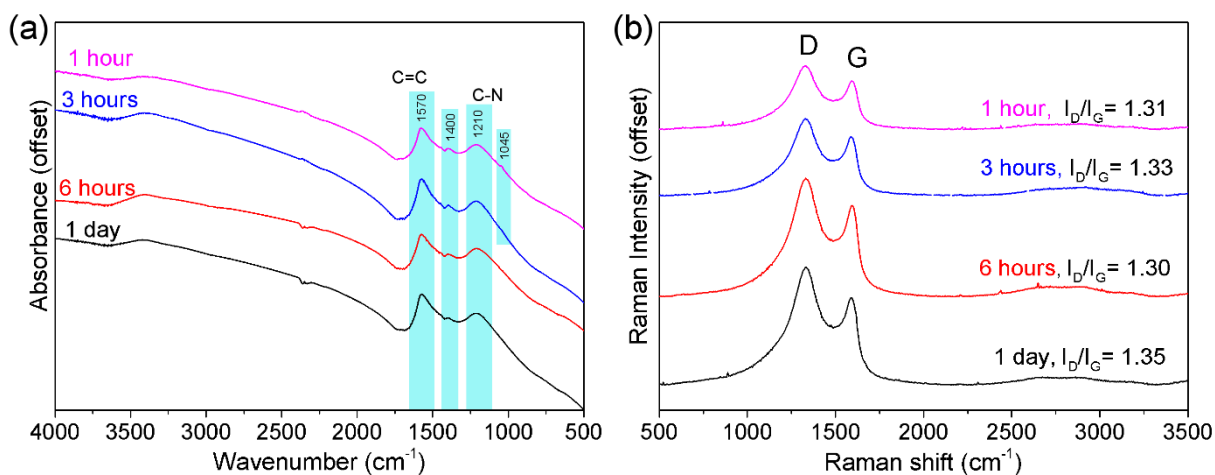


Figure S11. (a) FTIR and (b) Raman spectra of NG products obtained at different reaction times.

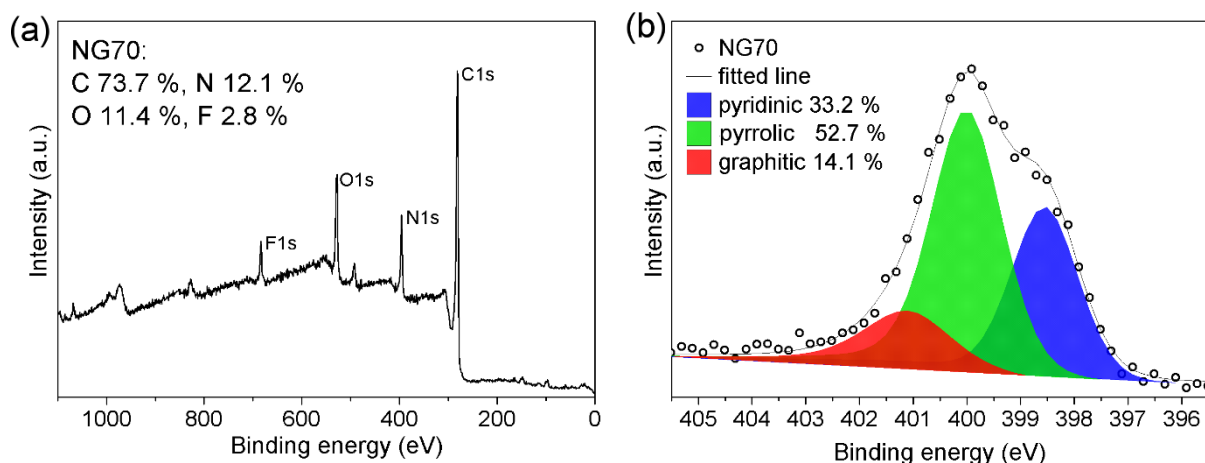


Figure S12. (a) Survey XPS spectrum of NG70 material and (b) its deconvoluted N 1s envelope.

The 1-day reaction performed at room temperature in DMF (NGrt product) showed a low nitrogen content (6.6 at. %), and the relative amounts of graphitic and pyridinic nitrogen (Figure S13a-b) were notably lower compared to the samples obtained at elevated temperatures. The annealing of the material at 1000 °C resulted in the drop of nitrogen content to 5 at. % (Figure S13c) with the N 1s XPS envelope showing that mainly graphitic and pyridinic nitrogens remained (Figure S13d). The presence of thermally stable nitrogen configurations in the NGrt material indicates that the N-doping occurs in small extent even at room temperature, which can be rationalized by the attack of NH_2^- on existing vacancies in the FG samples.

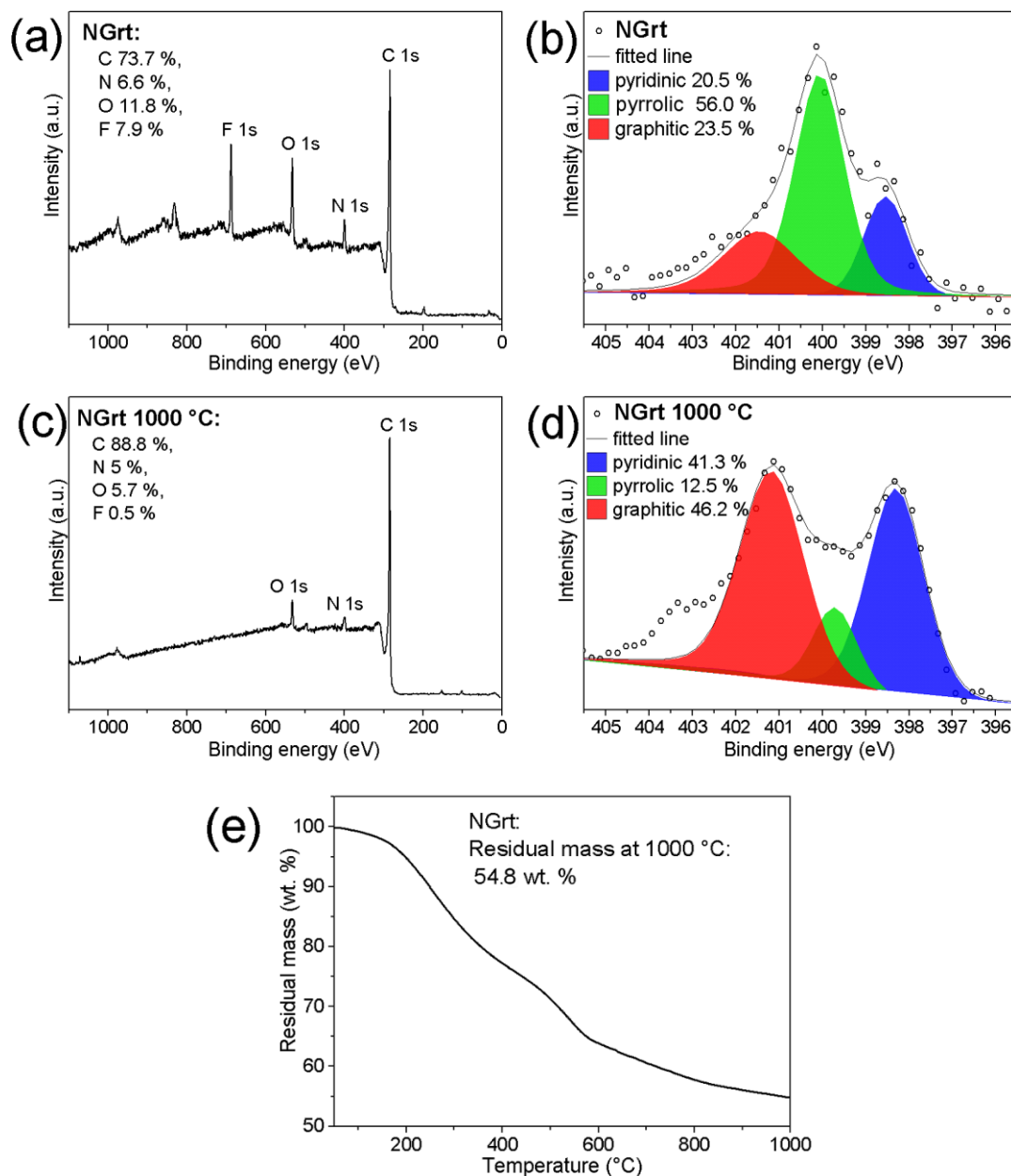


Figure S13. (a) Survey XPS spectrum of NGrt, (b) its deconvoluted N 1s envelope, (c) survey XPS spectrum on NGrt annealed to 1000 °C at a temperature ramp of 10 °C/min, (d) its deconvoluted N 1s envelope and (e) TGA curve corresponding to NGrt annealing.

Minor oxygen and nitrogen levels were present in the blank sample (FG treated by heating in DMF at 130 °C for 3 days, rFG), suggesting that atoms from solvent are also introduced into the material (Figure S14). However, the NG_ACN material also contained significant amounts of oxygen, suggesting that the oxygen may originate mainly from adventitious contamination from the environment.

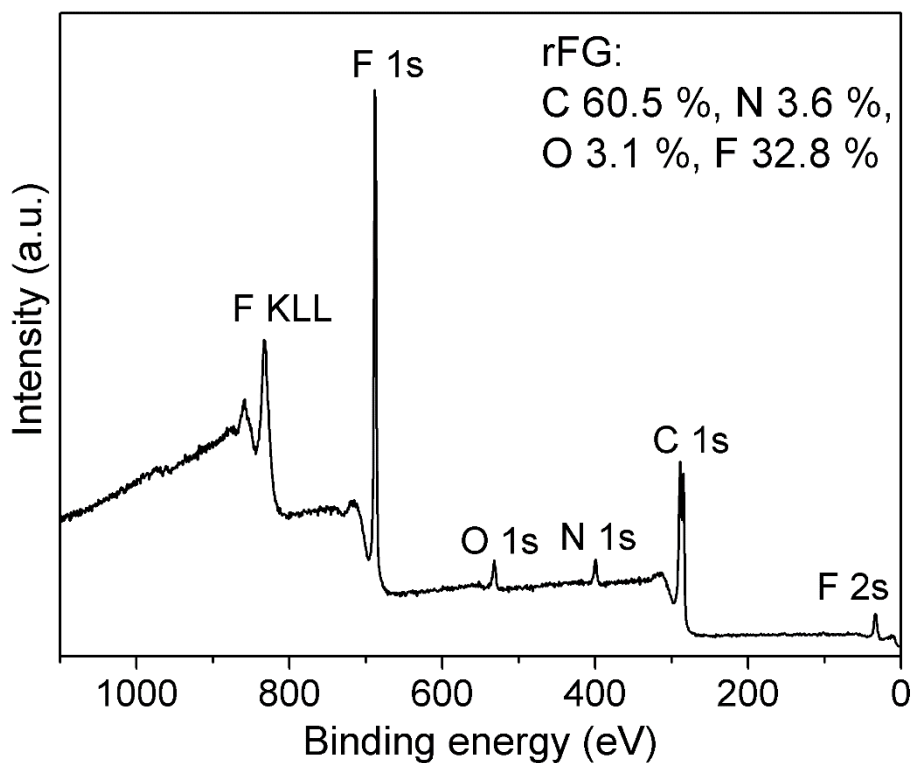


Figure S14. Survey spectrum of rFG; inset shows its elemental atomic composition.

5. Analysis and identification of water-soluble by-products washed out from the NG

All supernatants from NG washings were subjected to examination. The lyophilization of the first washing with water afforded a white powder (labeled NGwsb) in amounts enough for analysis. XRD of NGwsb revealed that its main component was sodium fluoride with a lower presence of sodium formate (Figure S15a). To examine the NGwsb sample further, Raman (Figure S15b) and FTIR (Figure S15c) spectra of the powder were collected. The FTIR spectrum showed a strong feature at 2250 cm^{-1} indicating stretching of $\text{-C}\equiv\text{N}$ group that was distinguishable in the Raman spectrum. By comparing Raman spectra of various nitrile compounds, sodium cyanate exhibited remarkably similar features in IR and Raman spectra. The FTIR spectrum of a well ground mixture of sodium cyanate and formate corresponded well with the FTIR spectrum of NGwsb, with minor differences. ^{13}C -NMR measurement (Figure S15d) only corroborated the presence of carbons in the formate and cyanate ions.

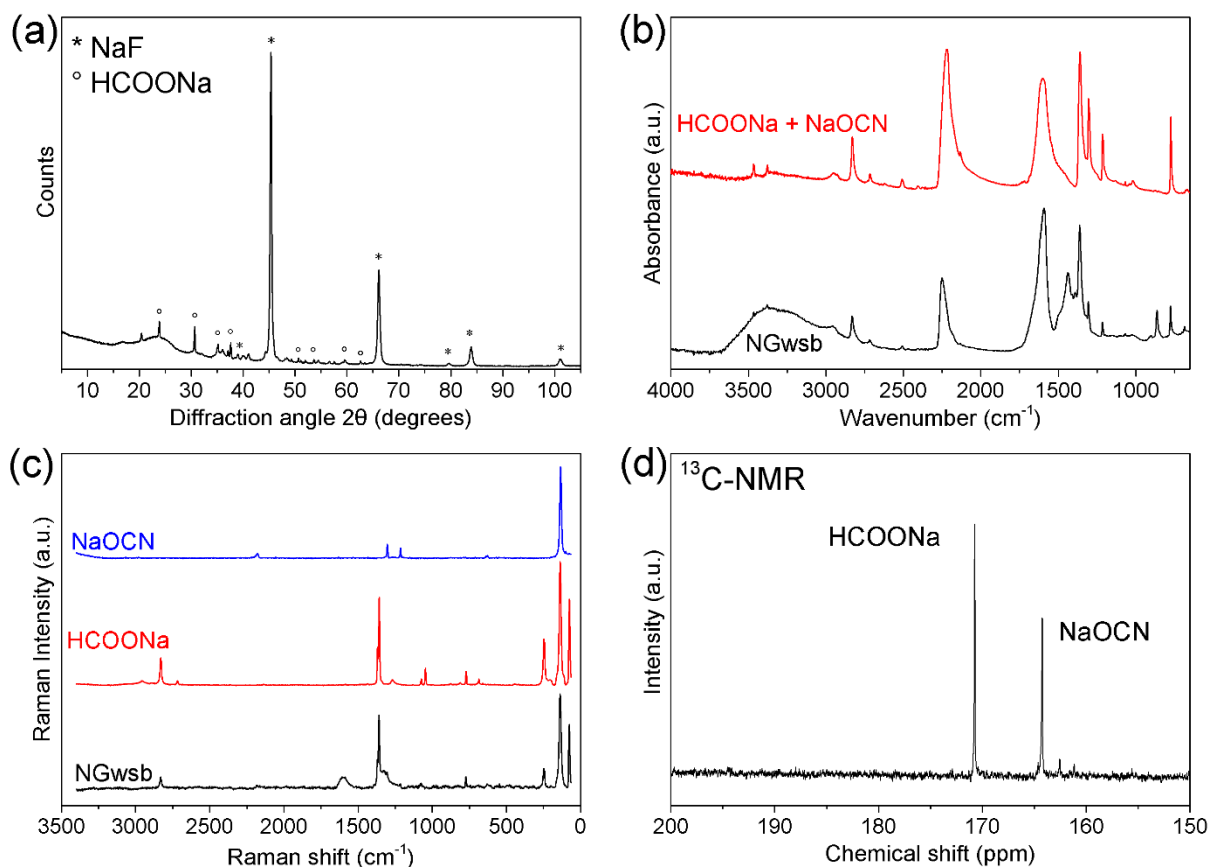


Figure S15. Identification of water-soluble byproducts in the NGwsb sample: (a) NGwsb X-ray diffractogram, (b) FTIR spectrum of NGwsb and its comparison with the spectrum of a mixture of sodium cyanate and sodium formate, (c) Raman spectrum of NGwsb and its comparison with spectra of sodium formate and cyanate, and (d) ¹³C-NMR spectrum of NGwsb water dispersion.

6. GC-MS analysis results

GC-MS analysis revealed the presence of many eluents, as can be seen on indicative chromatograms in Figures S16-19. The identified compounds based on the mass spectra are listed in Tables S1 and S2. As seen on the chromatogram of Figure S18, most components originated from the sodium amide reacting solely with DMF at 130 °C. Three of the eluents were impurities, specifically water, that originated from air moisture, *N,N*-dimethylacetamide, which was already present in stock anhydrous DMF, and the ortho-dichlorobenzene (oDCB), that was released from the used Teflon vessel during heating. Based on these findings, five compounds were ascribed to the reaction of DMF with NaNH₂: dimethylamine (DMA), dimethylaminoacetonitrile (DMAACN), tetramethylurea (TMU), dimethylurea (DMU) and formyltrimethylurea (FTMU). Although being formed solely by dispersing sodium amide in DMF, DMA content dramatically dropped as the reaction progressed. This might be due to its

gradual evaporation from the mixture since DMA is gas under normal conditions, or due to its participation in other side-reaction. TMU and DMAACN were present in all samples of experiments. However, while TMU presence spikes right after the start of the reaction and then it drops as the reaction progresses, DMAACN presence gradually increased as the reaction progressed with trend resembling increase of nitrogen content of the product or number of its pyridinic functionalities (Table S1, Figure 3b). DMAACN, although being formed during all tested reactions performed under elevated temperature, N-doping reactions exhibited significant contribution to its amount.

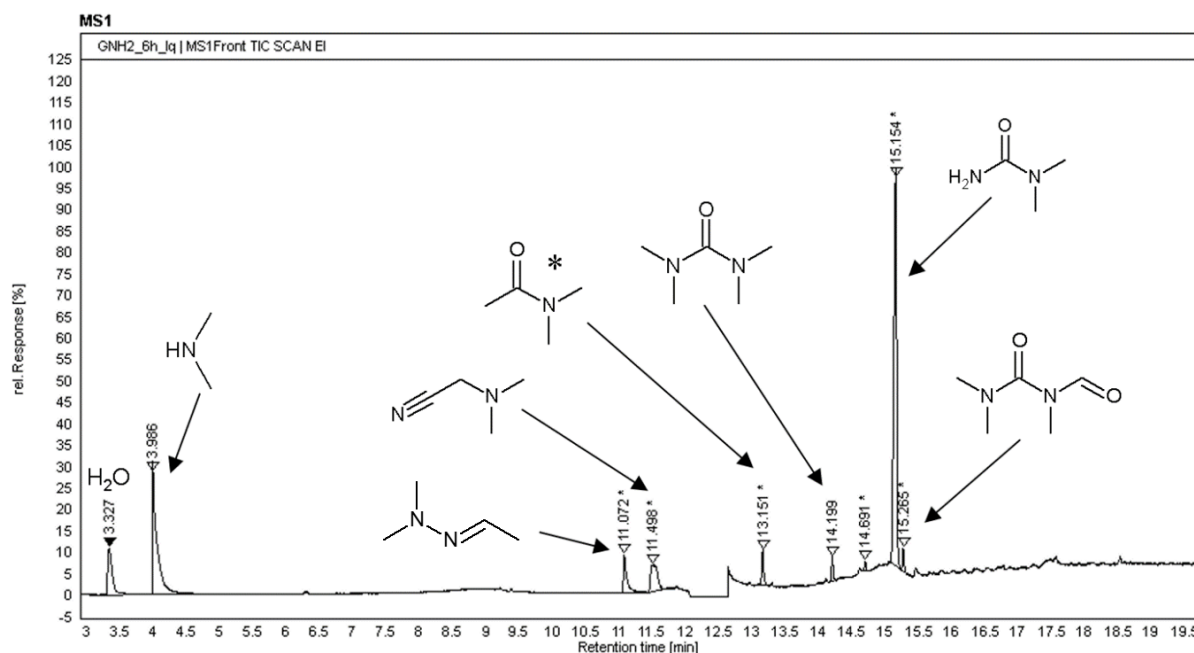


Figure S16. GC-MS chromatogram of DMF supernatant liquid from synthesis of NG (6 hours) with features assigned to corresponding identified compounds. Compounds with asterisk (*) are impurities.

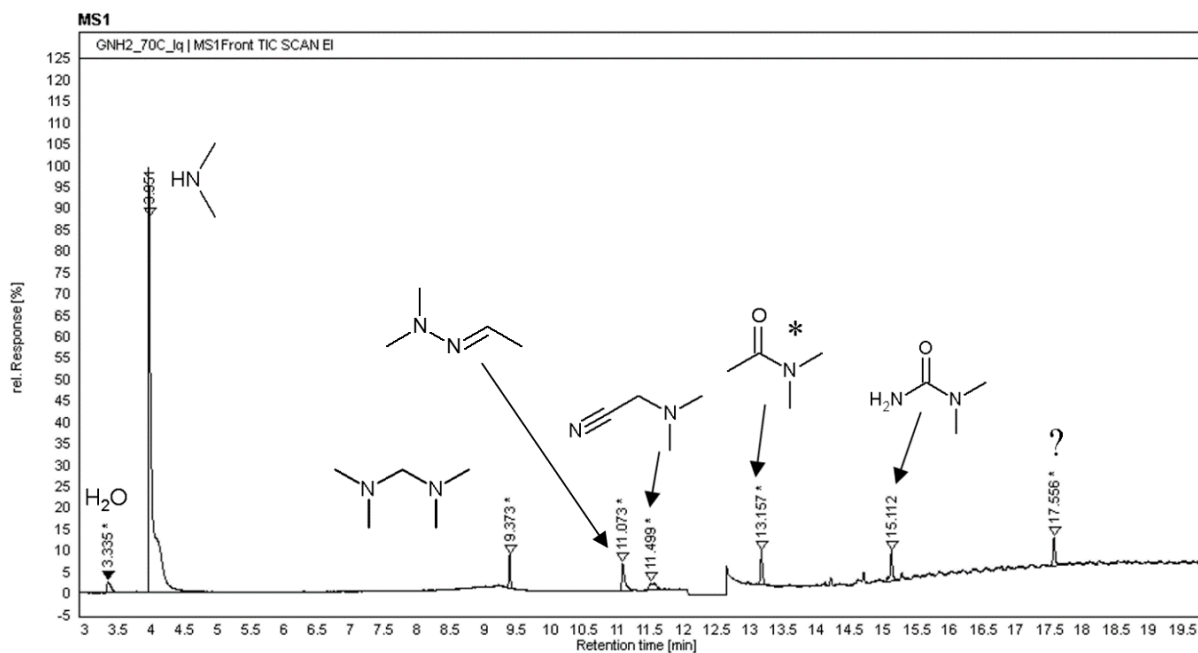


Figure S17. GC-MS chromatogram of DMF supernatant liquid from synthesis of NG70 with features assigned to corresponding identified compounds. Compounds with star (*) asterisk are impurities.

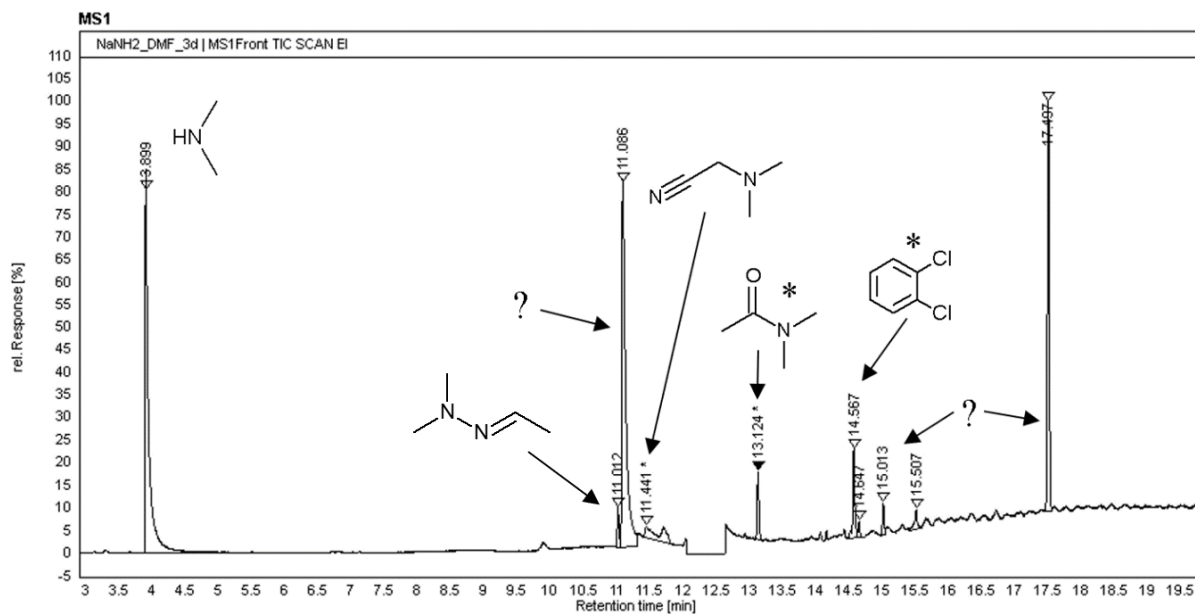


Figure S18. GC-MS chromatogram of DMF supernatant liquid from control reaction of NaNH_2 heated in DMF at 130 °C for 3 days with features assigned to corresponding identified compounds. Compounds with star (*) asterisk are impurities.

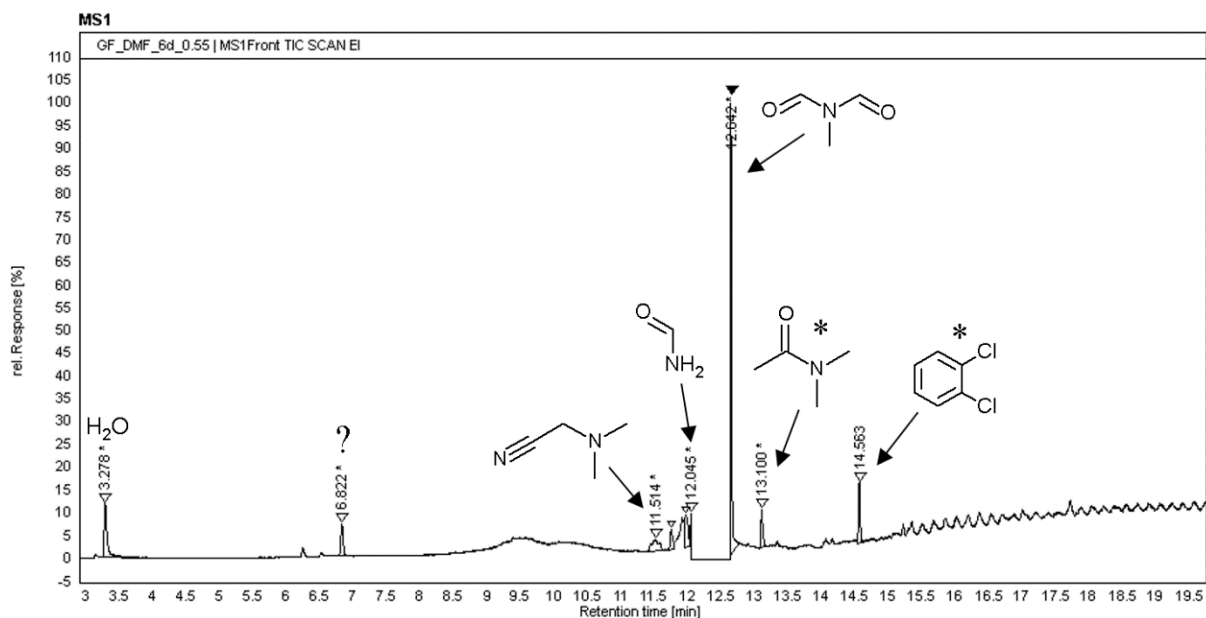


Figure S19. GC-MS chromatogram of DMF supernatant liquid from synthesis of rFG with features assigned to corresponding identified compounds. Compounds with star (*) asterisk are impurities.

Table S1. By-products of the reaction of GrF with NaNH₂ in DMF at 130 °C, which were soluble in the solvent of the reaction, and detected using GC-MS.

compound	Peak area *10 ⁶				
	1 hour	3 hours	6 hours	1 day	3 days
<chem>CN(C)</chem> dimethylamine	8.519	6.027	4.515	7.336	-
<chem>CN(C)N=CHCHO</chem> dimethylhydrazonacetaldehyde	1.490	1.678	0.949	1.735	0.641
<chem>CN(C)C#N</chem> dimethylaminoacetonitrile	1.163	1.524	1.360	3.448	4.739
<chem>CN(C)C(=O)N(C)C</chem> Tetramethylurea	1.408	0.372	0.288	0.229	0.139
<chem>CN(C)C(=O)N</chem> 1,1-dimethylurea	1.539	2.620	8.455	-	0.758
<chem>CN(C)C(=O)N=O</chem> formyltrimethylurea	0.279	0.398	0.271	-	0.266

Table S2. DMF-soluble compounds detected using the GC-MS from various reactions.

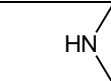
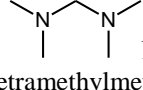
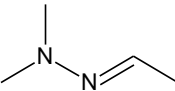
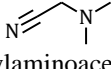
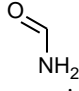
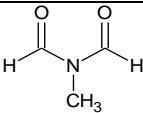
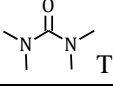
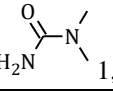
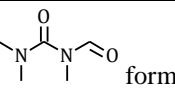
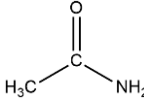
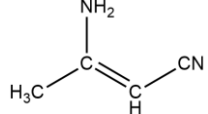
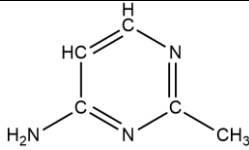
compound	Peak area *10 ⁶					
	DMF @130 °C	GF +DMF	DMF +NaNH ₂	DMF +NaNH ₂ @130 °C	NG70	NGrt
 dimethylamine	-	-	97.231	8.241	11.220	12.64
 N,N,N',N'- tetramethylmethanediamine (TMDA)	-	-	-	-	0.386	0.24
 dimethylhydrazoneacetaldehyde	-	-	-	0.436	0.641	-
 dimethylaminoacetonitrile	0.550	1.933	-	1.173	0.354	-
 formamide	-	0.302	-	-	-	-
 formylmethylformamide	4.334	3.502	-	-	-	-
 Tetramethylurea	-	-	-	-	0.139	-
 1,1-dimethylurea	-	-	-	-	0.758	-
 formyltrimethylurea	-	-	-	-	0.266	-

Table S3. Compounds detected using the GC-MS analysis of the supernatant taken from ACN-related reactions.

Retention time (min)	compound	Peak area * 10 ⁶	
		ACN+NaNH ₂ @r.t.	NG_ACN@70 °C
12.35	 acetamide	0.275	24.979
15.25	 3-aminocrotonitrile	30.044	62.819

16.37	 2,6-dimethyl-4-pyridinamine	20.071	49.266
-------	--	--------	--------

7. Supplementary data related to the reaction mechanism

Figure S20 shows an alternative reaction mechanism that could lead to formation of aziridinic N or to creation of new vacancy in FG lattice. The first reaction step, i.e. a nucleophilic attack of NH_2^- on point defect in FG, is favourable ($\Delta E_R = -62.1 \text{ kcal}\cdot\text{mol}^{-1}$, Figure S20 I. - II.) as we previously reported.¹⁴ The reaction proceeds by further dehydrogenation and defluorination accompanied by creation of a three-membered ring of aziridine ($\Delta E_R = -47.2 \text{ kcal}\cdot\text{mol}^{-1}$, Figure S20 II. - III.a or $\Delta E_R = -63.2 \text{ kcal}\cdot\text{mol}^{-1}$, Figure S22 II. – IV.). In the second case, dimethylamine radical (vide Scheme 1) may bind to the carbon atom in the vicinity of aziridine ring ($\Delta E_R = -36.3 \text{ kcal}\cdot\text{mol}^{-1}$, Figure S20 IV. - V.). Bonding of another NH_2^- to the carbon atom neighbouring to the newly created C-N bond causes a prominent buckling of the FG plane ($\Delta E_R = -30.3 \text{ kcal}\cdot\text{mol}^{-1}$, Figure S20 V. - VI.) and enables releasing of *N,N*-dimethylethyne-1,2-diamine, creation of a new vacancy in FG lattice, and aziridinic ring rearrangement into pyridinic nitrogen ($\Delta E_R = 7.8 \text{ kcal}\cdot\text{mol}^{-1}$, Figure S20 VI. - VII.). *N,N*-dimethylethyne-1,2-diamine further rearranges into dimethylacetonitrile ($\Delta E_R = -35.8 \text{ kcal}\cdot\text{mol}^{-1}$, Figure S20 VII.-VIII.) that was also observed experimentally in the reaction system (see Table S1). However, due to a high energy barrier of the *N,N*-dimethylethyne-1,2-diamine releasing (Figure S21 and S22) this mechanism seems to be improbable, and thus high content of incorporated N cannot be explained this way.

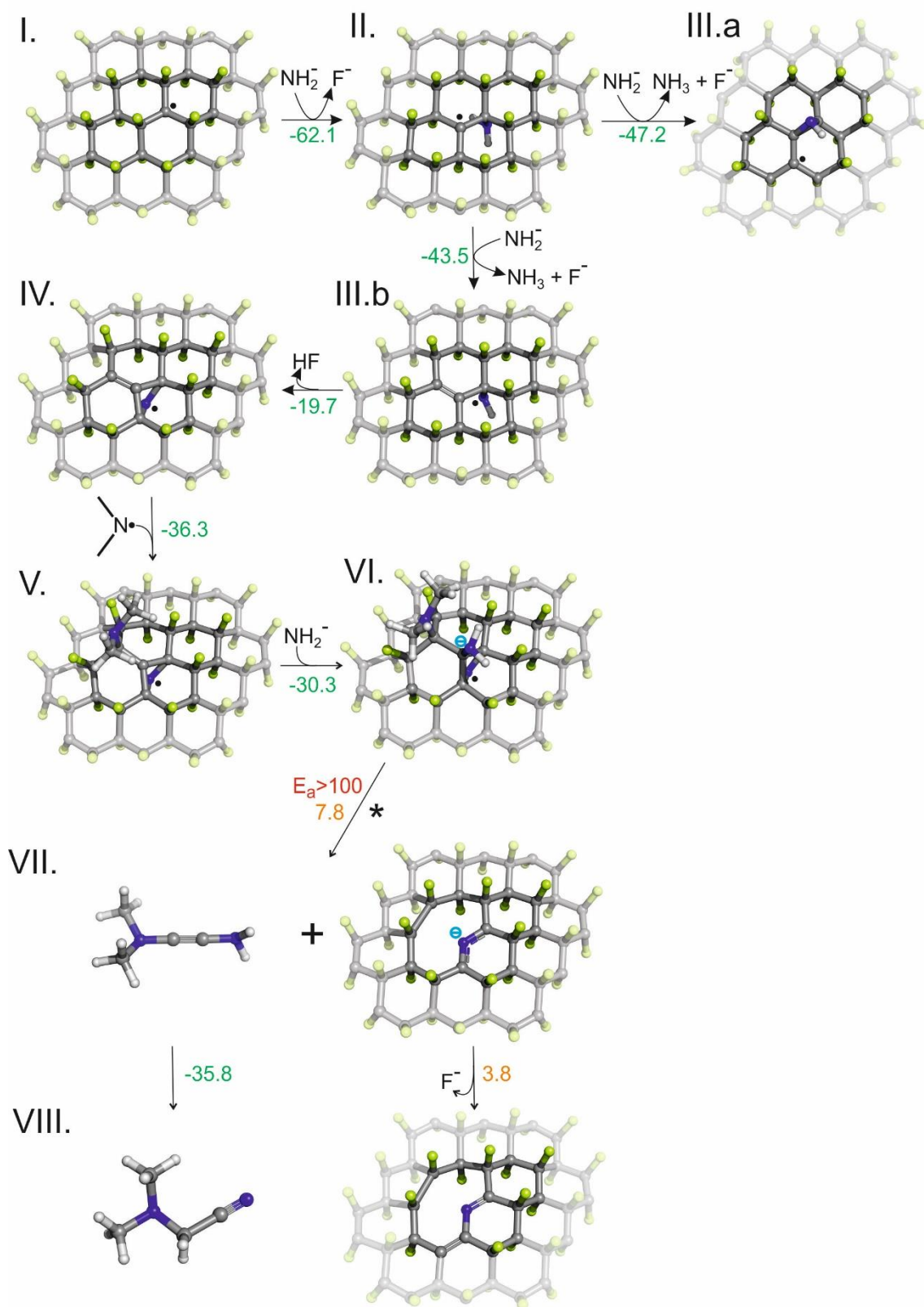


Figure S20. Nucleophilic attack of NH_2^- on a point defect in FG that may lead to a formation of aziridinic N (III.a) or creation of a vacancy in FG lattice (III.b and subsequent steps) accompanied by nitrogen incorporation that is caused by NH_2^- and dimethylamine radical

attachment and dimethylacetone nitrile release. Numbers correspond to the reaction energy values in $\text{kcal}\cdot\text{mol}^{-1}$. Carbon atoms are grey, fluorine green, nitrogen blue and hydrogen white

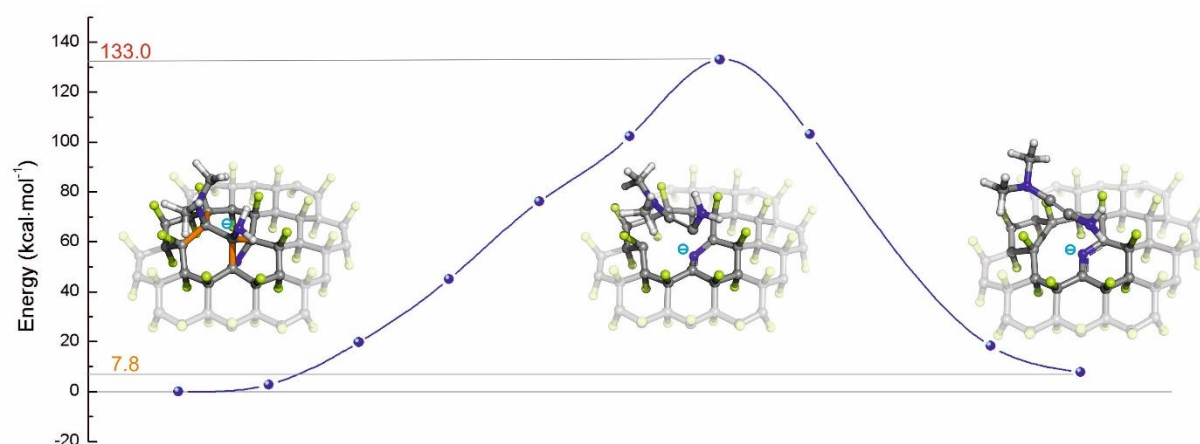


Figure S21. Energy profile of four C-C bonds (marked orange) dissociation in the step VI. – VII. of the reaction in S20 (marked with asterisk). Carbon atoms are grey, fluorine green, nitrogen blue and hydrogen white.

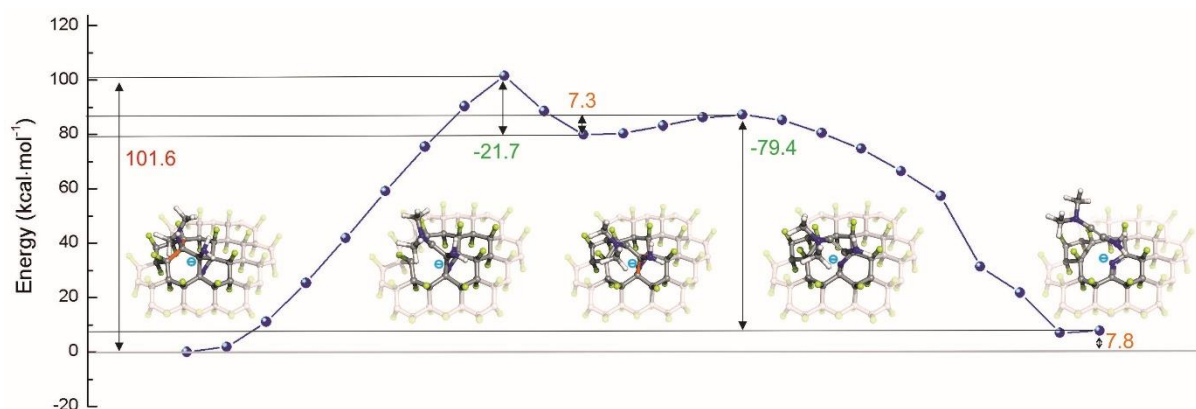


Figure S22. Energy profile of four C-C bonds (marked orange) dissociation in the step VI. – VII. of the reaction in S20 (marked with asterisk). Firstly, two C-C bonds near a DMA group are dissociated, then two C-C bonds near the NH_2 group are dissociated. Carbon atoms are grey, fluorine green, nitrogen blue and hydrogen white.

To identify the most probable defective structures in FG, we performed geometric optimizations of various FG structures containing vacancies. Figures S23-33 show considered structures divided according to the stoichiometry.

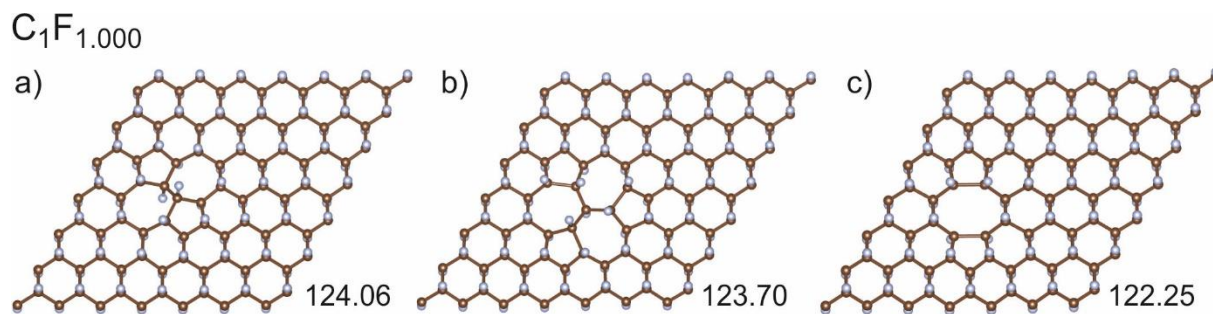


Figure S23. FG vacancies of C_1F_1 stoichiometry. a) SW(55-77), b) DV(555-777), c) DV(5-8-5). Carbon atoms are brown, fluorine grey. Cohesion energies are given in $\text{kcal}\cdot\text{mol}^{-1}$.

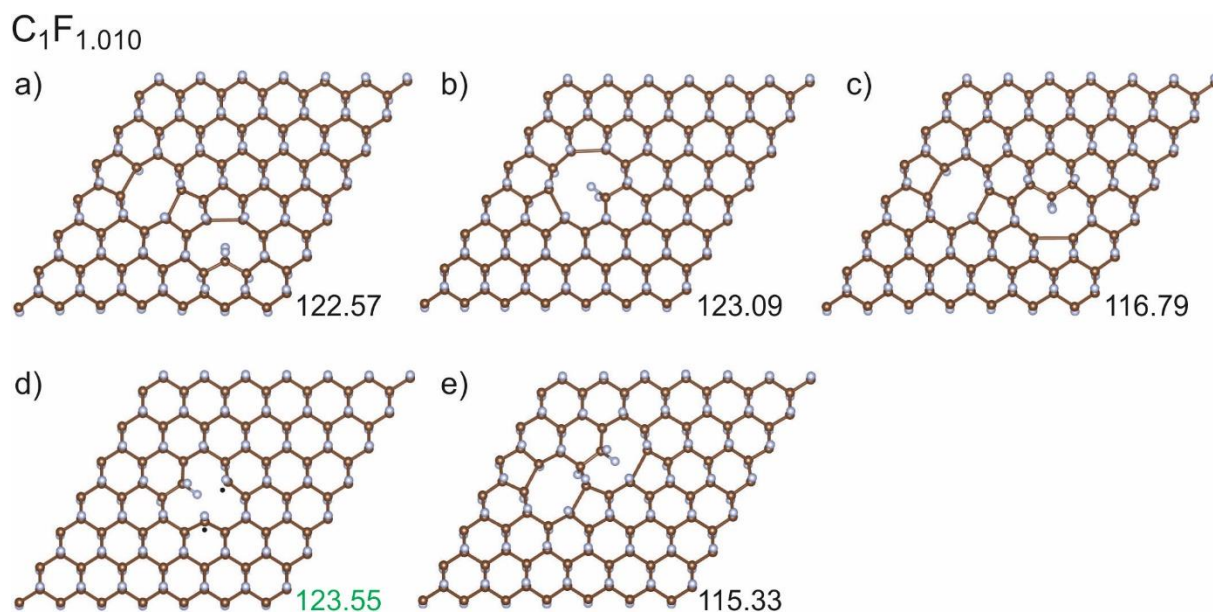


Figure S24. FG vacancies of $C_1F_{1.01}$ stoichiometry. a) TV(o-9), b) TV(o-1), c) TV(o-10), d) SV, e) TV(m-5). Carbon atoms are brown, fluorine grey. Cohesion energies are given in $\text{kcal}\cdot\text{mol}^{-1}$. Green number in d) highlight the third most stable vacancy (SV) that was used in N-incorporation calculations.

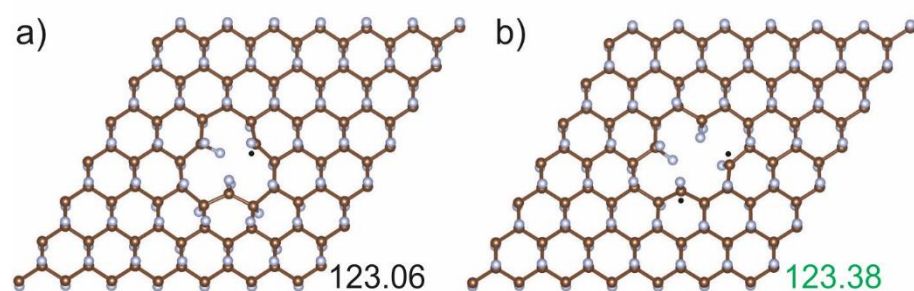


Figure S25. FG vacancies of $\text{C}_1\text{F}_{1.03}$ stoichiometry. a) SV, b) DV(14). Carbon atoms are brown, fluorine grey. Cohesion energies are given in $\text{kcal}\cdot\text{mol}^{-1}$. Green number in d) highlight the fourth most stable vacancy DV(14) that was used in N-incorporation calculations.

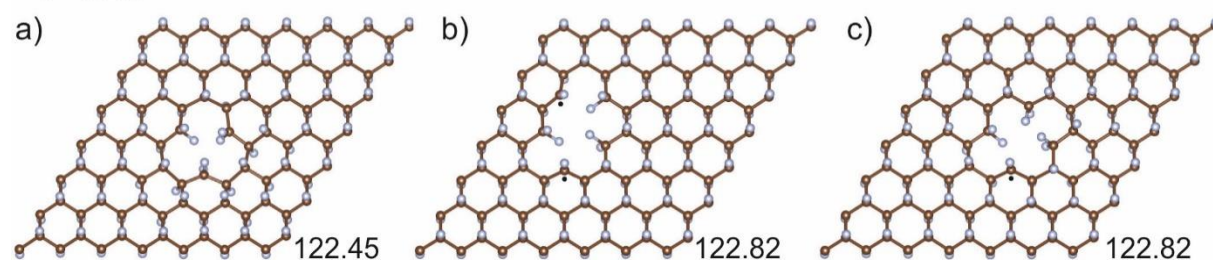


Figure S26. FG vacancies of $\text{C}_1\text{F}_{1.04}$ stoichiometry. a) SV, b) TV(o-1), c) DV(14). Carbon atoms are brown, fluorine grey. Cohesion energies are given in $\text{kcal}\cdot\text{mol}^{-1}$.

$C_1F_{1.060}$

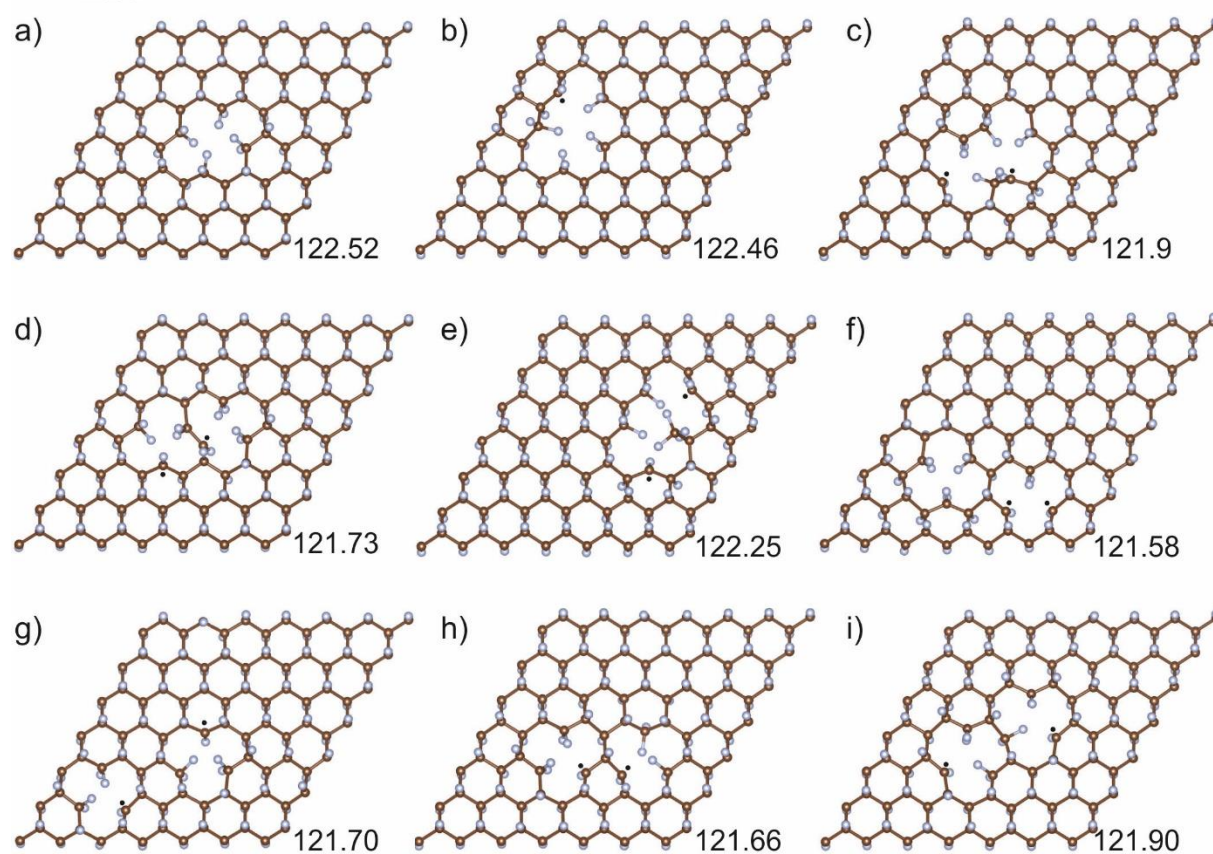


Figure S27. FG vacancies of $C_1F_{1.06}$ stoichiometry. a) DV(14), b) TV(o-1), c) DV(18), d) DV(12-12-a), e) DV(16), f) DV(12-12-b), g) DV(12-12-c), h) DV(12-12-d), i) DV(12-12-e). Carbon atoms are brown, fluorine grey. Cohesion energies are given in $\text{kcal}\cdot\text{mol}^{-1}$.

$C_1F_{1.070}$

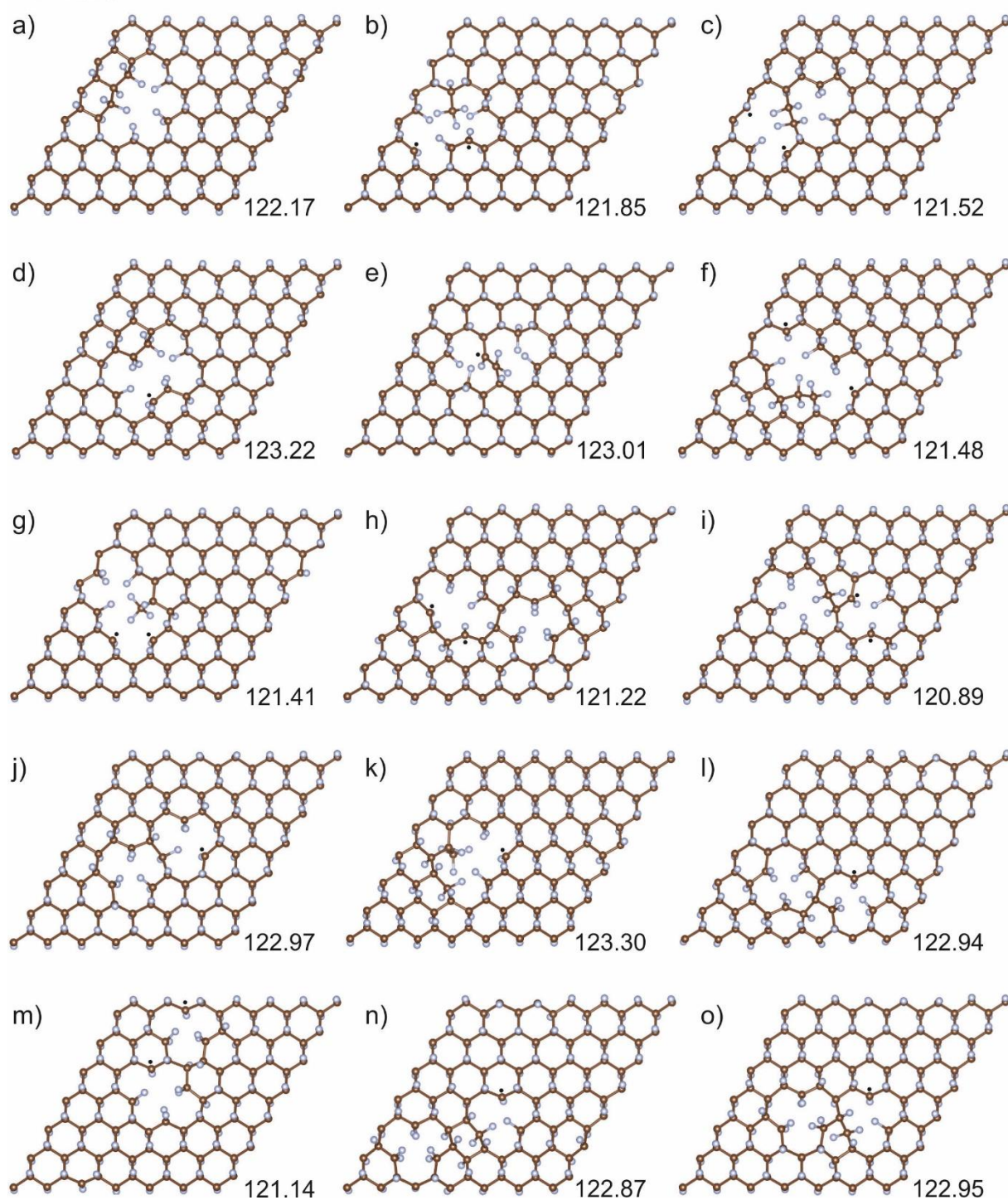


Figure S28. FG vacancies $C_1F_{1.07}$ stoichiometry. a) TV(o-1), b) TV(o-2), c) TV(o-3), d) DV(18), e) DV(12-12-a), f) TV(o-4), g) TV(o-5), h) TV(o-10), i) TV(o-11), j) DV(12-12-e), k) DV(16), l) DV(12-12-b), m) TV(o-8), n) DV(12-12-c), o) DV(12-12-d). Carbon atoms are brown, fluorine grey. Cohesion energies are given in $\text{kcal}\cdot\text{mol}^{-1}$.

$C_1F_{1.085}$

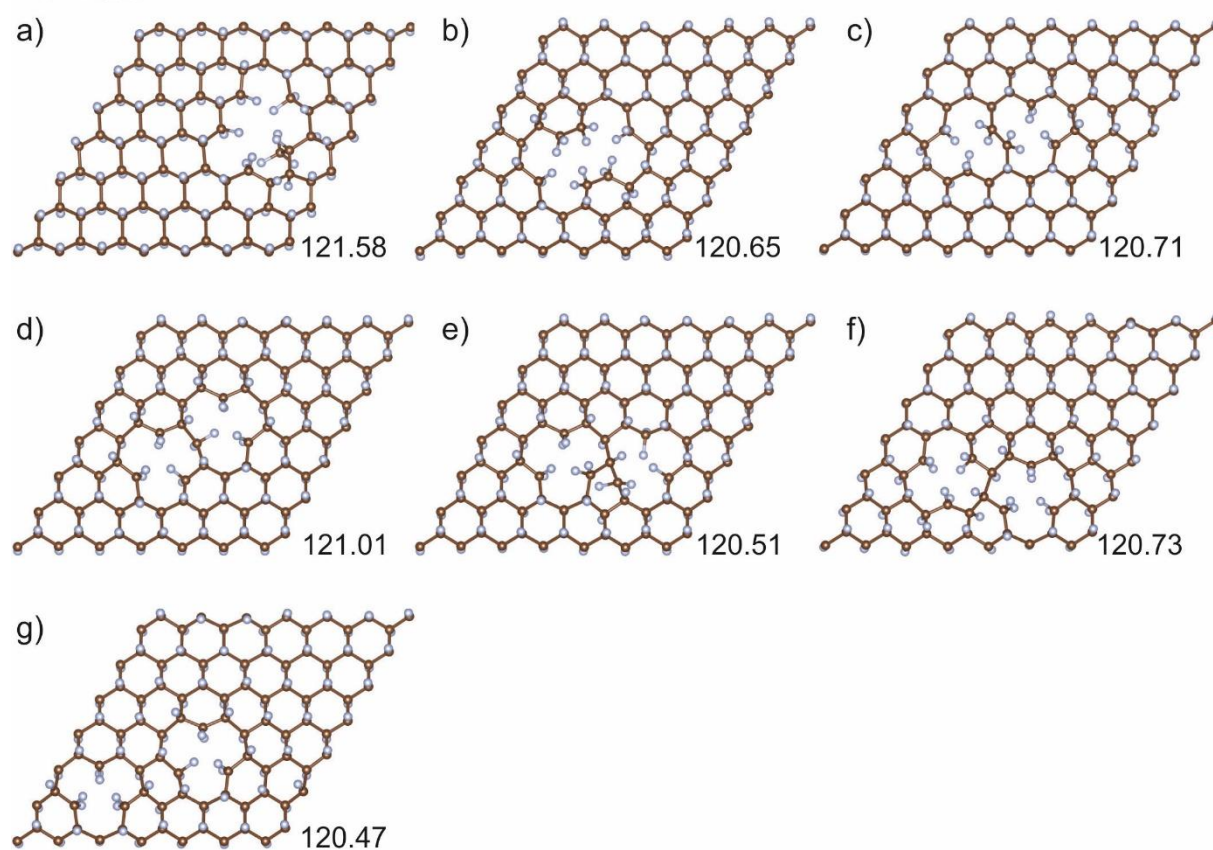


Figure S29. FG vacancies $C_1F_{1.085}$ stoichiometry. a) DV(16), b) DV(18), c) DV(12-12-a), d) DV(12-12-e), e) DV(12-12-d), f) DV(12-12-b), g) DV(12-12-c). Carbon atoms are brown, fluorine grey. Cohesion energies are given in $\text{kcal}\cdot\text{mol}^{-1}$.

$C_1F_{1.090}$

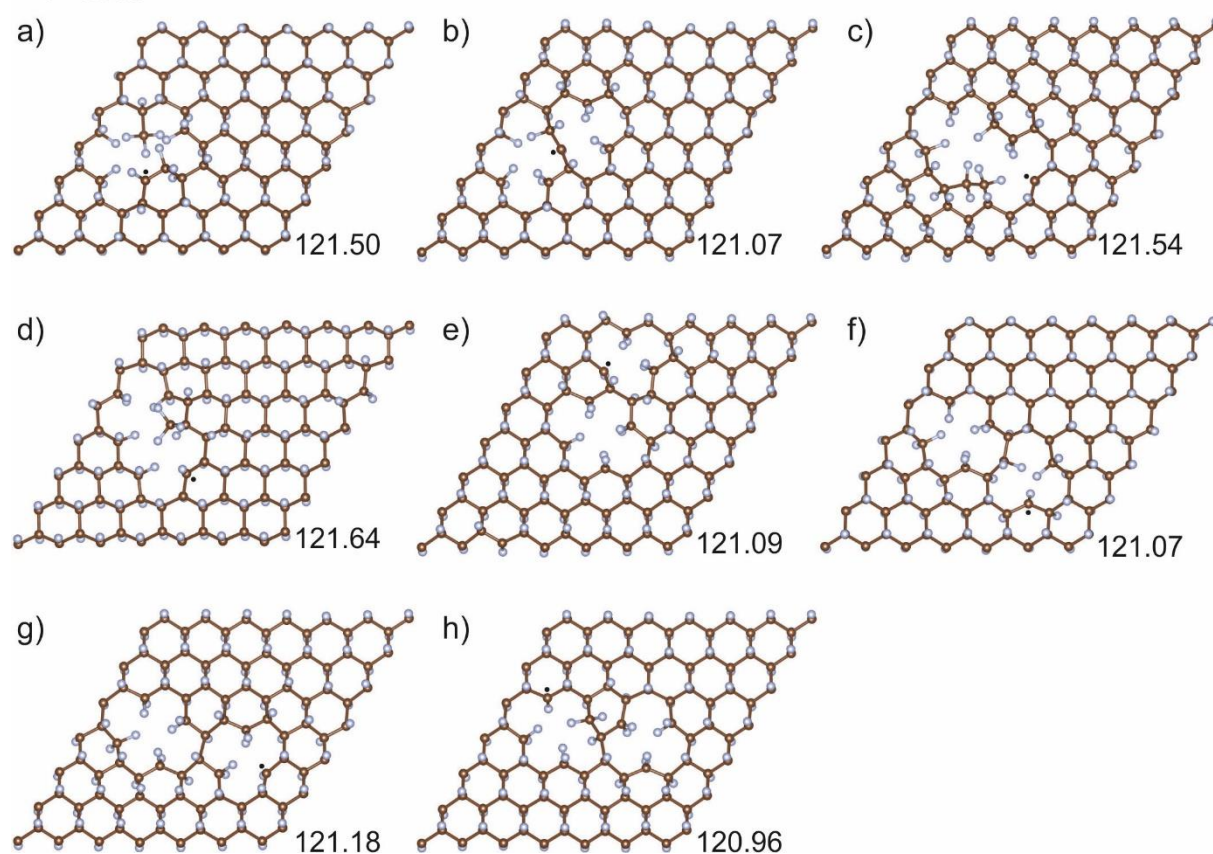


Figure S30. FG vacancies $C_1F_{1.09}$ stoichiometry. a) TV(o-2), b) TV(o-3), c) TV(o-4), d) TV(o-5), e) TV(o-8), f) TV(o-9), g) TV(o-10), h) TV(o-11). Carbon atoms are brown, fluorine grey. Cohesion energies are given in $\text{kcal}\cdot\text{mol}^{-1}$.

$C_1F_{1.100}$

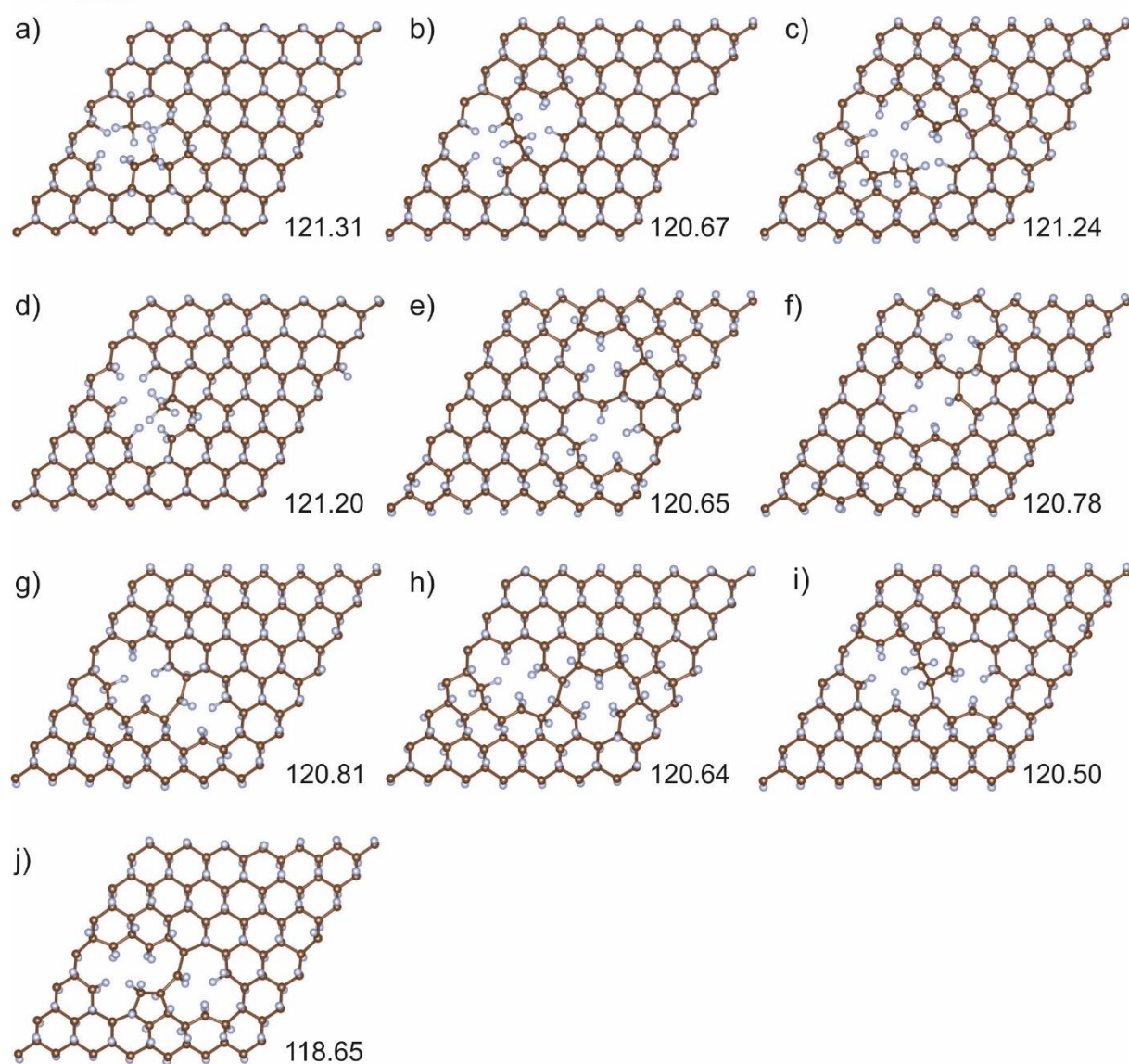


Figure S31. FG vacancies $C_1F_{1.1}$ stoichiometry. a) TV(o-2), b) TV(o-3), c) TV(o-4), d) TV(o-5), e) TV(o-7), f) TV(o-8), g) TV(o-9), h) TV(o-10), i) TV(o-11), j) TV(m-12). Carbon atoms are brown, fluorine grey. Cohesion energies are given in $\text{kcal}\cdot\text{mol}^{-1}$.

$C_1F_{1.120}$

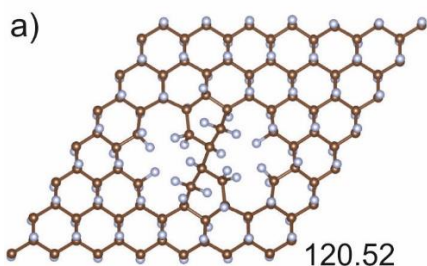


Figure S32. FG vacancies $C_1F_{1.12}$ stoichiometry. a) QV(14-14). Carbon atoms are brown, fluorine grey. Cohesion energies are given in $\text{kcal}\cdot\text{mol}^{-1}$.

$C_1F_{1.130}$

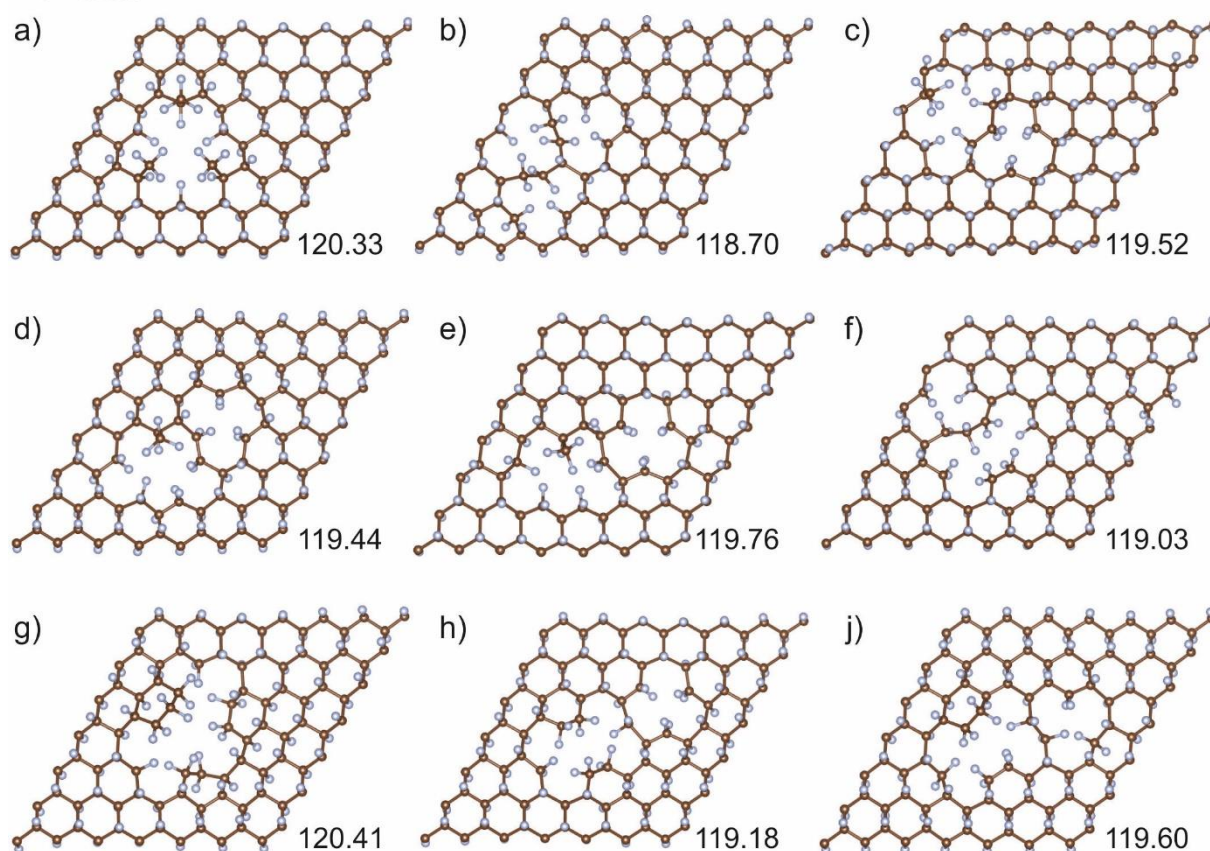


Figure S33. FG vacancies $C_1F_{1.13}$ stoichiometry. a) TV(m-1), b) TV(s), c) TV(m-6), d) TV(m-10), e) TV(m-11), f) TV(p-1), g) TV(p-2), h) TV(p-3), j) TV(p-4). Carbon atoms are brown, fluorine grey. Cohesion energies are given in $\text{kcal}\cdot\text{mol}^{-1}$.

The surface area and pore size analysis showed surface pore expansion during the reaction (Figure S7). Therefore, we also considered a scenario that might lead to an expansion of FG vacancies (Figure S34). This reaction mechanism is also initialized by NH_2^- attachment

and release of F^- ($\Delta E_R = -38.8 \text{ kcal}\cdot\text{mol}^{-1}$, Figure S34 I.-II.). The next step is a slightly unfavourable nucleophilic attack ($\Delta E_R = 2.4 \text{ kcal}\cdot\text{mol}^{-1}$, Figure S34 II.-III.) of DMA anion (see Scheme 1) on the carbon neighbour to the newly created C-N bond accompanied by releasing of another F^- . The vacancy is then expanded by release of *N,N*-dimethylethyne-1,2-diamine that is rearranged into DMAACN ($\Delta E_R = -27.7 \text{ kcal}\cdot\text{mol}^{-1}$, Figure S34 III.-IV.) which was observed experimentally (Table S1, S2, Figure S16-19).

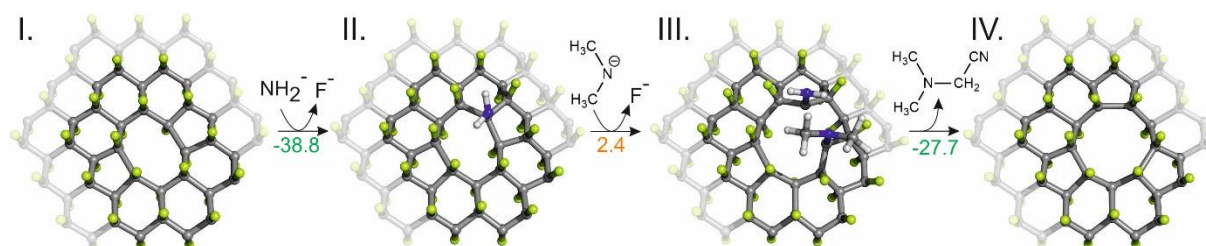
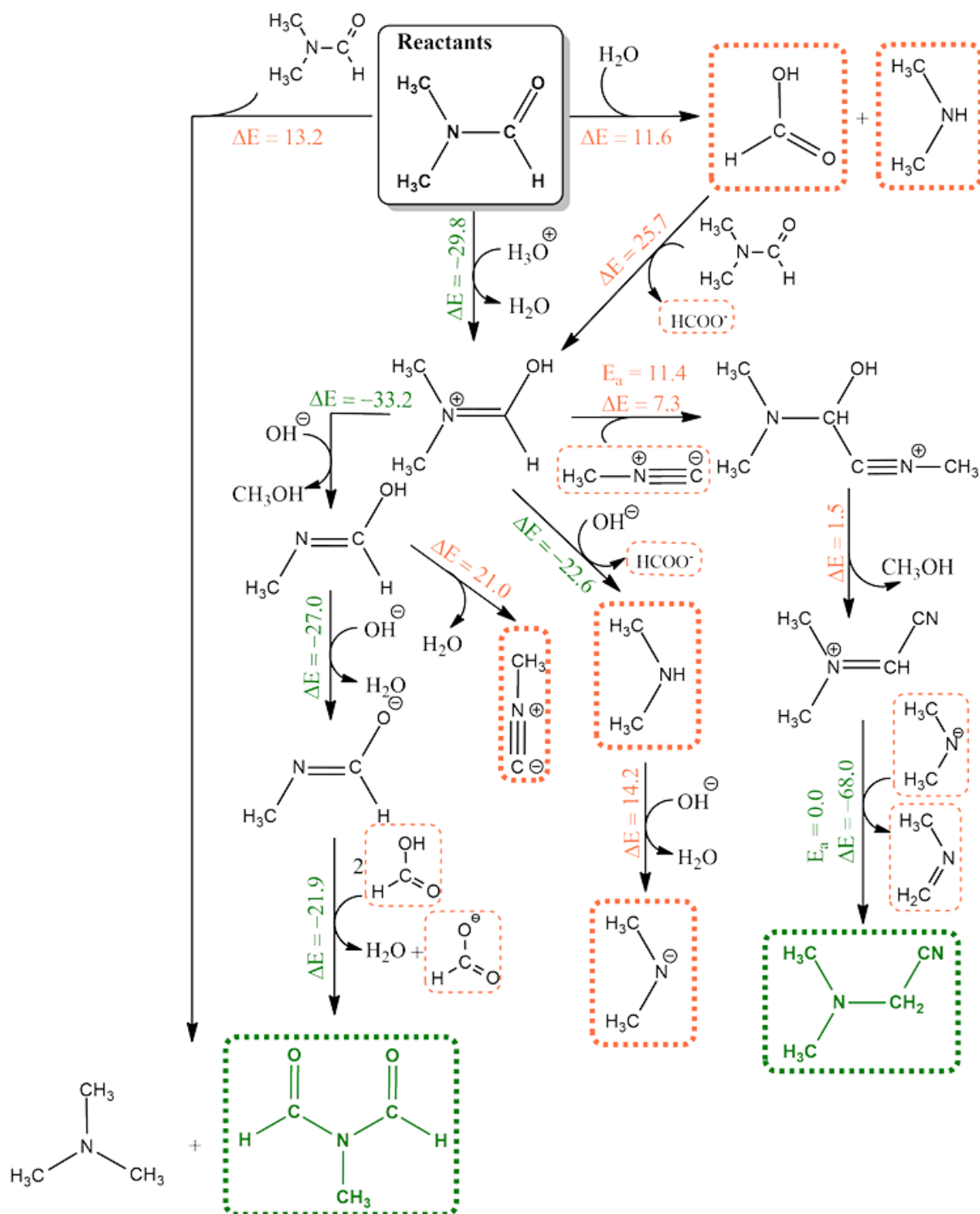


Figure S34. NH_2^- nucleophilic attack on double vacancy DV(5-8-5) (step I. - II.) and subsequent nucleophilic attack by DMA anion (step II. – III.) that leads to expansion of the vacancy and release of DMAACN (step III. – IV.). Carbon atoms are grey, fluorine green, nitrogen blue and hydrogen white. Reaction energies are in $\text{kcal}\cdot\text{mol}^{-1}$.

To explain the formation of various by-products that were observed experimentally (GC-MS), we performed multiple calculations. Scheme S1 shows possible reaction scenarios that may occur in *N,N*-dimethylformamide at elevated temperatures. We have considered also reactions of DMF with water since experimental data show presence of small amount of water in our samples. Scheme S2 shows possible side-reactions in the system of DMF+FG. Scheme S3 shows more comprehensively than Scheme 1 possible side-reactions in DMF+FG+NaNH₂. Scheme S4 shows possible side-reactions in ACN+NaNH₂.

Possible side-reactions in DMF

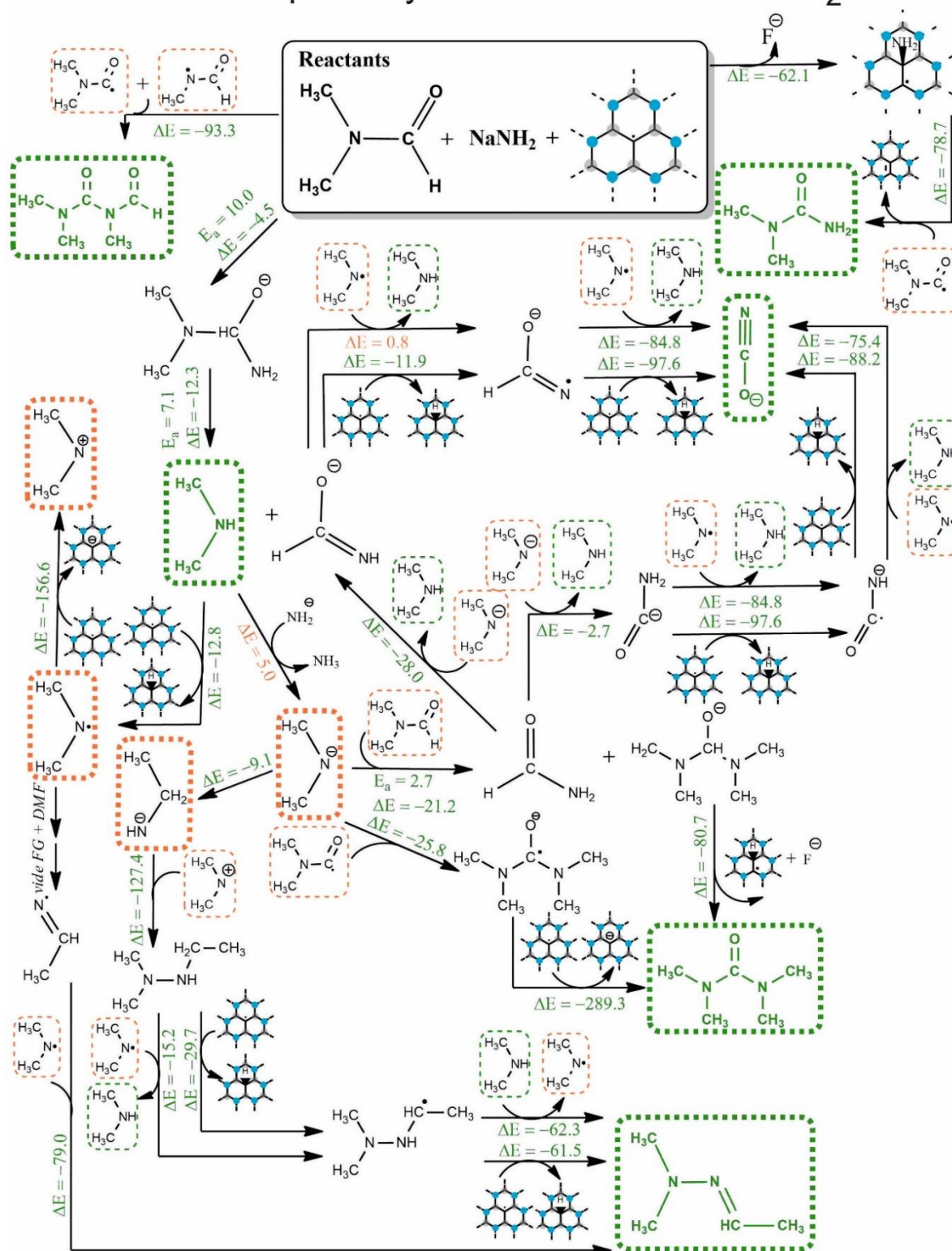


Scheme S1. Possible reaction pathways in DMF. Products in green frames were observed experimentally by GC-MS. Products in orange frames play important roles in other reactions that take place in DMF system or in other considered systems (Scheme 1, S2 and S3). E_a is the energy barrier, ΔE is the reaction energy. All values are in $\text{kcal}\cdot\text{mol}^{-1}$.

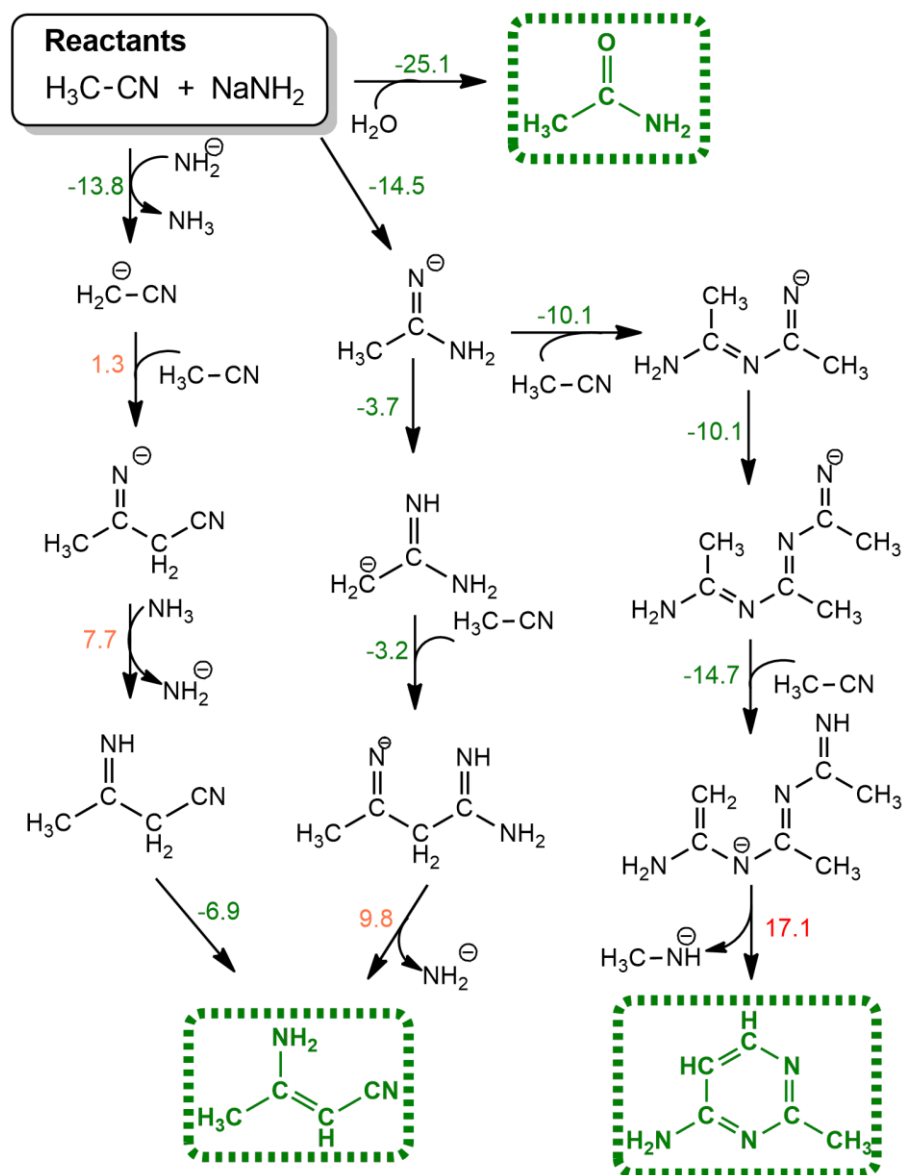
[illegible]

S34

Possible reaction pathways in FG mixed with NaNH₂ in DMF



Scheme S3. Possible reaction pathways for FG and NaNH₂ mixed in DMF. Products in green frames were observed experimentally by GC-MS, Raman and FT-IR. Products in orange frames play important roles in other reactions that take place in DMF + FG system or in other considered systems (Scheme 1). E_a is the energy barrier and ΔE is the reaction energy in kcal·mol⁻¹.



Scheme S4. Possible reactions of NaNH_2 and ACN . Products in green frames were observed experimentally by GC-MS (see Table S3). Reaction energies are in kcal·mol⁻¹.

References

1. Grimme, S. Semiempirical GGA-type density functional constructed with a long-range dispersion correction. *J. Comput. Chem.* **2006**, 27 (15), 1787-1799, DOI 10.1002/jcc.20495.
2. Blöchl, P. E. Projector augmented-wave method. *Phys. Rev. B* **1994**, 50 (24), 17953-17979, DOI 10.1103/PhysRevB.50.17953.
3. Kresse, G. and Furthmüller, J. Efficient iterative schemes for ab initio total-energy calculations using a plane-wave basis set. *Phys. Rev. B* **1996**, 54 (16), 11169-11186, DOI 10.1103/PhysRevB.54.11169.
4. Kresse, G. and Furthmüller, J. Efficiency of ab-initio total energy calculations for metals and semiconductors using a plane-wave basis set. *Comp. Mater. Sci.* **1996**, 6 (1), 15-50, DOI 10.1016/0927-0256(96)00008-0.
5. Kresse, G. and Joubert, D. From ultrasoft pseudopotentials to the projector augmented-wave method. *Phys. Rev. B* **1999**, 59 (3), 1758-1775, DOI 10.1103/PhysRevB.59.1758.

6. Monkhorst, H. J. and Pack, J. D. Special points for Brillouin-zone integrations. *Phys. Rev. B* **1976**, 13 (12), 5188-5192, DOI 10.1103/PhysRevB.13.5188.
7. Blum, V., Gehrke, R., Hanke, F., Havu, P., Havu, V., Ren, X., Reuter, K. and Scheffler, M. Ab initio molecular simulations with numeric atom-centered orbitals. *Comput. Phys. Commun.* **2009**, 180 (11), 2175-2196, DOI 10.1016/j.cpc.2009.06.022.
8. Perdew, J. P., Burke, K. and Ernzerhof, M. Generalized gradient approximation made simple. *Phys. Rev. Lett.* **1996**, 77 (18), 3865-3868, DOI 10.1103/PhysRevLett.77.3865.
9. Frisch, M. J., et al. Gaussian 09. **2016**, Wallingford CT, Gaussian, Inc.
10. Chai, J.-D. and Head-Gordon, M. Long-range corrected hybrid density functionals with damped atom-atom dispersion corrections. *Phys. Chem. Chem. Phys.* **2008**, 10 (44), 6615-6620, DOI 10.1039/b810189b.
11. Ditchfield, R., Hehre, W. J. and Pople, J. A. Self-Consistent Molecular-Orbital Methods. IX. An Extended Gaussian-Type Basis for Molecular-Orbital Studies of Organic Molecules. *J. Chem. Phys.* **1971**, 54 (2), 724-728, DOI 10.1063/1.1674902.
12. Marenich, A. V., Cramer, C. J. and Truhlar, D. G. Universal Solvation Model Based on Solute Electron Density and on a Continuum Model of the Solvent Defined by the Bulk Dielectric Constant and Atomic Surface Tensions. *J. Phys. Chem. B* **2009**, 113 (18), 6378-6396, DOI 10.1021/jp810292n.
13. Dubecky, M., Otyepkova, E., Lazar, P., Karlicky, F., Petr, M., Cepe, K., Banas, P., Zboril, R. and Otyepka, M. Reactivity of Fluorographene: A Facile Way toward Graphene Derivatives. *J. Phys. Chem. Lett.* **2015**, 6 (8), 1430-1434, DOI 10.1021/acs.jpcllett.5b00565.
14. Matochová, D., Medved', M., Bakandritsos, A., Steklý, T., Zbořil, R. and Otyepka, M. 2D Chemistry: Chemical Control of Graphene Derivatization. *J. Phys. Chem. Lett.* **2018**, 9 (13), 3580-3585, DOI 10.1021/acs.jpcllett.8b01596.